UNIVERSITY OF CALIFORNIA
RIVERSIDE

Fabrication and Characterization of Nanoscale Pillar Arrays With Engineered Phononic and Photonic Properties

A Dissertation submitted in partial satisfaction
of the requirements for the degree of

Doctor of Philosophy

in

Materials Science and Engineering

by

Chun Yu Tammy Huang

December 2019

Dissertation Committee:
Dr. Fariborz Kargar, Co-Chairperson
Dr. Alexander A. Balandin, Co-Chairperson
Dr. Aleksandr Khitun

The Dissertation Chun Yu Tammy Huang is approved:

_____

_____

Committee Co-Chairperson

_____

Committee Co-Chairperson

University of California, Riverside

Acknowledgements

I would like to express my greatest gratitude to my dissertation advisors, Dr. Fariborz Kargar, dissertation director, and Dr. Alexander A. Balandin, Ph.D. committee co-chair, for their guidance through my research. I would like to thank Dr. Balandin granting me the opportunity and freedom to conduct research under his supervision and involving me in different fields of study. Thank you for giving me many opportunities to attend conferences and internships to meet many experts in the field. More importantly, I would like to thank Dr. Kargar spending so much time and energy to train me to do better than ever during your busy schedules, thank you for giving me the opportunities to learn from you. Indeed, their enthusiasm and intellect encouraged me to carry on my graduate study even at the times of disappointment. I hope I had a part in giving the group some values. I also would like to thank Dr. Alexander Khitun for serving as members of my dissertation committee. I was very fortunate to collaborate with him during my graduate program.

Many thanks to Dr. Bishwajit Debnath and Topojit Debnath from Dr. Roger Lake's research group. Without them, I could have not fulfilled the theoretical part of my experimental findings. Hope we can continue our findings together and build a stronger friendship. I would also like to express my gratitude to current members of the Nano Device Laboratory (NDL) and the center for Phonon Optimized Engineered Materials (POEM). I would personally like to thank Dr. Ruben Salgado for being the first member to welcome me into the group and kindly mentored me throughout the first few months. His guidance during my first quarter studies immensely helped me to push my project through. Without

the help of my colleagues at Phonon Optimized Engineered Materials (POEM) Center and Dr. Dong Yan at Center for Nanoscale Science & Engineering, I could not have completed my research. Thank you all for your help and support.

My sincerest gratitude goes to my dearest friend Lizet Huerta and Luis for the great support and patience during this journey. I would also like to thank my friends, without their friendships to reach to the end of this road would be impossible. I wish to acknowledge the mentorship of Dr. Glen Birdwell. I also sincerely appreciate the support and advice from many other members of the Electronic Technology Branch; CCDC-ARL: Dr. Dmitry Ruzmetov, Dr. Mahesh Neupane, Mr. James Weil, Dr. Kevin Crawford, Dr. Pankaj Shah, and Dr. Tony Ivanov. Also, many thanks to Mike Valentin, Sina Najmaei, Alex Mazzoni, Matt Chin for the help. I would also like to acknowledge support from DOD HBCU/MI Summer Program for the support.

Finally, I would like to give my profound thanks to my family who supported me throughout my studies especially to my mother. Without their love and dedication, to reach to the end of this road would be impossible. I love you all so much and thank you for being there for me no matter what happens.

To my parents

ABSTRACT OF THE DISSERTATION

Fabrication and Characterization of Nanoscale Pillar Arrays With Engineered Phononic and Photonic Properties

by

Chun Yu Tammy Huang

Doctor of Philosophy, Graduate Program in Materials Science and Engineering
University of California, Riverside, December 2019
Dr. Fariborz Kargar, Dr. Alexander A. Balandin, Co-Chairpersons

This dissertation reports the results of the investigation of nanoscale pillar structures with engineered phononic and photonic properties. It has been proven that phonon states in semiconductors can be tuned by external boundaries, either as a result of phonon confinement effects in individual nanostructures or as a result of artificially induced external periodicity, e.g., phononic crystals. The possibility of engineering acoustic phonon spectrum is of ultimate importance from scientific and application perspectives since they are the main heat carriers in nonmagnetic semiconductor and insulator materials. The change in acoustic phonon dispersion would affect the heat transport properties, alter the electron-phonon interactions, and affect the optical properties of the material system. It has been recently suggested that periodic structures with properly tuned dimensions can act simultaneously as phononic and photonic crystals, strongly affecting the light-matter interactions. In this dissertation research, I prepared nanoscale pillar structure samples and

investigated their properties. The “pillar with hat” structures were fabricated using electron beam lithography on silicon substrates followed by inductively-coupled plasma cryogenic dry etching. The hats of the pillars were created with a unique design to have exactly the same orientation plane as the substrate. The structures were inspected with scanning electron microscopy. I used Brillouin-Mandelstam spectroscopy to measure the dispersion of acoustic phonons with energies in the range from 2 GHz up to 20 GHz through the entire second and higher order Brillouin zones. I analyzed the spectral signatures resulting from the surface ripple mechanism which dominates the light scattering in these specific samples. I found clear signatures of the phonon spectrum modification in the appearance of localized phonon sub-bands at energies between 2-20 GHz. The variable angle ellipsometry measurements indicated modification of light scattering due to nanostructuring. The experimental data confirmed the dual functionality of the structure with engineered phononic-photonic properties. The results obtained in this dissertation research have important implications for the next generation of photonic and optoelectronic device technologies.

Contents

List of Figures

Chapter 1 Introduction

1.1 Motivation

Phoxonic crystals (PxC) are referred to as artificial materials, which exhibit simultaneous modulation of the elastic and electromagnetic properties within a single structure as a result of externally induced periodic boundaries [1–4]. One can consider PxC to be a structure with a concurrent dual functionality of the *phononic* crystals (PnC) and *photonic* crystals (PtC). Separately, PnCs [5–8] and PtCs [9–12] have been the subjects of intense theoretical and experimental investigations for the past two decades. Despite differences in intended applications, the structures share common physical characteristics. In PnC, a periodic modulation of the elastic constants and mass density define the phonon propagation while in PtC a periodic modulation of the dielectric constants define the photon propagation. The PnC and PtC arrays are tailored through construction of periodic lattices of holes or pillars, or a combination of both, with fine-tuned dimensions and unit cells. Since modulation of visible light and acoustic phonons of a certain energy range both require structure dimensions on the order of a few hundreds of nanometers one can envision a structure with the dual phonon – photon functionality. A proper selection of the periodic structure, with contrasting acoustic and optical properties, as well as a specific design of the lattice geometry and dimensions set up the common platform for PxCs, where novel phonon and photon characteristics and enhanced light-matter interactions are observed [13–15]. This

approach has already been utilized in designing new types of optoelectronic devices such as phoxonic sensors [16–18] and optomechanical cavities [13,19].

Engineering the phonon states of materials, *i.e.* changing the phonon properties by imposing spatial confinement in individual [20–23] or by inducing artificial periodicity as in PnCs [5–8], has proven to be beneficial for thermal management, particularly at low temperatures [24–27], acoustic filtering [28], and wave guiding [29] applications. Acoustic phonons are the main heat carriers in electrically insulating and semiconducting materials, contribute strongly to the electron-phonon interactions in technologically important materials [30–33], and participate in the non-radiative generation-recombination processes [34]. The external periodicity of the pillar-based PnCs, additional to the crystal atomic periodicity, results in the zone-folding of acoustic phonons, and appearance of the new *quasi-optical* phonon polarization branches with non-zero energy at the Brillouin zone (BZ) center ($\omega(q = 0) \neq 0$) [35,36]. The properties of quasi-optical phonons are substantially different from those of the fundamental longitudinal acoustic (LA) and transverse acoustic (TA) phonons, which have zero energy at the BZ center ($\omega(q = 0) = 0$) and a linear dispersion close to the BZ center. The quasi-optical phonons are similar to the true optical phonons but have the energies much lower than the optical phonons. The quasi-optical phonon modes are generally characterized by the hybridized vibrational displacement profiles. These modes change the phonon density of states (PDOS), and influence the thermal transport, especially at low temperatures, where the wave nature of phonons starts to dominate the phonon scattering processes. Generally, it is believed that the thermal conductivity in thin-film PnCs reduces due to nanostructuring [24,25,37]. However, a

recent theoretical study suggested that the thermal conductivity can be increased at low temperatures via fine-tuning of PnC dimensions and nanopatternings [24,25].

Tuning the phonon dispersion in the PnC structures and in individual nanostructures can affect the optical and electrical properties of the material. Engineering the dispersion in PnCs in such a way that the phonon DOS attains its maximum or minimum within the energy required to trigger the carrier transition between the defect, *i.e.* trapping state and the conduction or valence band can result in either enhanced or suppressed G-R center recombination [38]. A recent experimental study found that modification of the phonon dispersion in the core-shell $GaAs_{0.7}Sb_{0.3}$/InP nano-pillar arrays affects the hot carrier relaxation in such structures [39]. In another example, opening up a band gap in a certain phonon frequency range with an accurate design of the hole PnCs can strongly influence the quasiparticle recombination lifetime in a superconductor [40].

The periodic modulation of the dielectric constant in PtCs can lead to localization of electromagnetic waves, *e.g.*, visible light, of a certain frequency range. In PtCs, a photonic energy stop band or a complete band gap can emerge, suppressing the electromagnetic wave propagation [10]. A common criterion for designing PtCs is utilization of the periodic structures with materials of the highest contrast in the refractive index [10]. Conventionally, PtCs, similar to PnCs, are fabricated in two configurations – the arrays of the air-holes [41] or the lattices of the pillars [42]. In the pillar-based structures, silicon nano-pillars are fabricated on a layer of a low refractive index material, *e.g.* SiO_2, to minimize the optical damping by the substrate [43]. However, recent studies demonstrated silicon-on-silicon PtCs with symmetric spheroidal-like nano-pillars, which are optically separated from the

substrate and have low optical losses [44]. The coexistence of localized phonon and photon modes in these structures enhance the light-matter interaction, which can be beneficial for certain photonic, optoelectronic, or optomechanical devices [13].

In this dissertation, we report the results of Brillouin-Mandelstam spectroscopy (BMS) and variable angle spectroscopic ellipsometry (VASE) of the nanoscale "pillar with hat" periodic silicon structures. The innovative idea of the study is to engineer the shape of the nanoscale pillar array in such a way that the phonon spectrum undergoes modification both due to periodicity of the arrays and phonon localization in the "hats" of the pillars. The larger diameters of the "hats" than that of the pillars are expected to result in better elastic decoupling from the substrates and resonant effects promoting acoustic phonon localization. From the other side, the periodicity of the structure was selected in the range ensuring the structure acts as both PnC and PtC. Our results confirm the interplay of the localization and periodicity effects for phonons, as well the dual phonon and light functionality of the shape-engineered nano-pillar arrays. The described approach increases the range of tuning parameters available for optimization of PxC performance.

1.2 Outline of the Dissertation

The rest of the dissertation is organized as follows:

- ***Chapter 2:*** the basics and fundamentals of Brillouin-Mandelstam spectroscopy (BMS) will be discussed. BMS is a non-destructive optical tool used for probing

acoustic phonons in transparent and opaque materials. In this chapter, the BMS experimental setup and the mechanisms which contribute to the light scattering by phonons will be reviewed. We also will demonstrate the applicability of BMS spectroscopy on different material systems. It will be demonstrated that BMS can efficiently observe acoustic phonons in various materials and nanostructured materials.

- ***Chapter 3:*** the procedure for fabrication and characterization of special types of nanostructured materials with engineered phononic and photonic properties – named "pillar with hat" – will be explained.
- ***Chapter 4:*** we will present the results of BMS spectroscopy and variable angle spectroscopic ellipsometry on these structures. It will be discussed that in "pillar with hat" structures not only phonon states experience significant modifications, but also the dielectric constant, and thus the optical response of the material undergoes notable changes in the range of visible light wavelengths and present the summary and conclusions of our findings.

References:

[1] Y. El Hassouani, C. Li, Y. Pennec, E.H. El Boudouti, H. Larabi, A. Akjouj, O. Bou Matar, V. Laude, N. Papanikolaou, A. Martinez, B. Djafari-Rouhani, Dual phononic and photonic band gaps in a periodic array of pillars deposited on a thin plate, Phys. Rev. B. 82 (2010) 155405. https://doi.org/10.1103/PhysRevB.82.155405.

[2] Y. Pennec, B. Djafari-Rouhani, E.H. El Boudouti, C. Li, Y. El Hassouani, J.O. Vasseur, N. Papanikolaou, S. Benchabane, V. Laude, A. Martinez, Simultaneous existence of phononic and photonic band gaps in periodic crystal slabs, Opt. Express. 18 (2010) 14301. https://doi.org/10.1364/OE.18.014301.

[3] E. Alonso-Redondo, H. Huesmann, E.H. El Boudouti, W. Tremel, B. Djafari-Rouhani, H.J. Butt, G. Fytas, Phoxonic hybrid superlattice, ACS Appl. Mater. Interfaces. 7 (2015) 12488–12495. https://doi.org/10.1021/acsami.5b01247.

[4] B. Djafari-Rouhani, S. El-Jallal, Y. Pennec, Phoxonic crystals and cavity optomechanics, Comptes Rendus Phys. 17 (2016) 555–564. https://doi.org/10.1016/J.CRHY.2016.02.001.

[5] M. Sledzinska, B. Graczykowski, J. Maire, E. Chavez-Angel, C.M. Sotomayor-Torres, F. Alzina, 2D phononic crystals: Progress and prospects in hypersound and thermal transport engineering, Adv. Funct. Mater. (2019) 1904434. https://doi.org/10.1002/adfm.201904434.

[6] Y. Pennec, B. Djafari-Rouhani, Fundamental properties of phononic crystal, in: Phononic Cryst., Springer New York, New York, NY, 2016: pp. 23–50. https://doi.org/10.1007/978-1-4614-9393-8_2.

[7] Y. Xiao, Q. Chen, D. Ma, N. Yang, Q. Hao, Phonon transport within periodic porous structures — from classical phonon size effects to wave effects, ES Mater. Manuf. 5 (2019) 2–18. https://doi.org/10.30919/esmm5f237.

[8] M.I. Hussein, M.J. Leamy, M. Ruzzene, Dynamics of phononic materials and

structures: Historical origins, recent progress, and future outlook, Appl. Mech. Rev. 66 (2014) 040802–1. https://doi.org/10.1115/1.4026911.

[9] E. Yablonovitch, Inhibited spontaneous emission in solid-state physics and electronics, Phys. Rev. Lett. 58 (1987) 2059–2062. https://doi.org/10.1103/PhysRevLett.58.2059.

[10] E. Yablonovitch, Photonic band-gap crystals, J. Phys. Condens. Matter. 5 (1993) 2443–2460. https://doi.org/10.1088/0953-8984/5/16/004.

[11] T. Baba, Slow light in photonic crystals, Nat. Photonics. 2 (2008) 465–473. https://doi.org/10.1038/nphoton.2008.146.

[12] S. Pirandola, B.R. Bardhan, T. Gehring, C. Weedbrook, S. Lloyd, Advances in photonic quantum sensing, Nat. Photonics. 12 (2018) 724–733. https://doi.org/10.1038/s41566-018-0301-6.

[13] M. Eichenfield, J. Chan, R.M. Camacho, K.J. Vahala, O. Painter, Optomechanical crystals, Nature. 462 (2009) 78–82. https://doi.org/10.1038/nature08524.

[14] P.-A. Mante, L. Belliard, B. Perrin, Acoustic phonons in nanowires probed by ultrafast pump-probe spectroscopy, Nanophotonics. 7 (2018) 1759–1780. https://doi.org/10.1515/nanoph-2018-0069.

[15] P.-A. Mante, N. Anttu, W. Zhang, J. Wallentin, I.-J. Chen, S. Lehmann, M. Heurlin, M.T. Borgström, M.-E. Pistol, A. Yartsev, Confinement effects on Brillouin scattering in semiconductor nanowire photonic crystal, Phys. Rev. B. 94 (2016) 024115. https://doi.org/10.1103/PhysRevB.94.024115.

[16] R. Lucklum, M. Zubtsov, A. Oseev, Phoxonic crystals-a new platform for chemical and biochemical sensors, Anal. Bioanal. Chem. 405 (2013) 6497–6509. https://doi.org/10.1007/s00216-013-7093-9.

[17] A. Martínez, Phoxonic crystals: tailoring the light-sound interaction at the nanoscale, in: Photonic Phononic Prop. Eng. Nanostructures III, SPIE, 2013: p. 86320W. https://doi.org/10.1117/12.2013340.

[18] Y. Pennec, R. Moiseyenko, B.D. Rouhani, S. Amoudache, R. Tigrine, R. Lucklum, A. Khater, Sensing light and sound velocities of fluids in 2D phoxonic crystal slab, in: Proc. IEEE Sensors, Institute of Electrical and Electronics Engineers Inc., 2014: pp. 355–357. https://doi.org/10.1109/ICSENS.2014.6985007.

[19] M. Aspelmeyer, T.J. Kippenberg, F. Marquardt, Cavity optomechanics, Rev. Mod. Phys. 86 (2014) 1391–1452. https://doi.org/10.1103/RevModPhys.86.1391.

[20] J. Zou, A. Balandin, Phonon heat conduction in a semiconductor nanowire, J. Appl. Phys. 89 (2001) 2932–2938. https://doi.org/10.1063/1.1345515.

[21] A.A. Balandin, D.L. Nika, Phononics in low-dimensional materials, Mater. Today. 15 (2012) 266–275. https://doi.org/https://doi.org/10.1016/S1369-7021(12)70117-7.

[22] E.P. Pokatilov, D.L. Nika, A.A. Balandin, Acoustic phonon engineering in coated cylindrical nanowires, Superlattices Microstruct. 38 (2005) 168–183. https://doi.org/10.1016/j.spmi.2005.06.001.

[23] A.A. Balandin, Nanophononics: Phonon engineering in nanostructures and nanodevices, J. Nanosci. Nanotechnol. 5 (2005) 1015–1022. https://doi.org/10.1166/jnn.2005.175.

[24] R. Anufriev, M. Nomura, Heat conduction engineering in pillar-based phononic crystals, Phys. Rev. B. 95 (2017) 155432. https://doi.org/10.1103/PhysRevB.95.155432.

[25] R. Anufriev, M. Nomura, Thermal conductance boost in phononic crystal nanostructures, Phys. Rev. B. 91 (2015) 245417. https://doi.org/10.1103/PhysRevB.91.245417.

[26] R. Anufriev, A. Ramiere, J. Maire, M. Nomura, Heat guiding and focusing using ballistic phonon transport in phononic nanostructures, Nat. Commun. 8 (2017) 15505. https://doi.org/10.1038/ncomms15505.

[27] R. Lucklum, Phononic crystals and metamaterials - Promising new sensor platforms, in: Procedia Eng., Elsevier Ltd, 2014: pp. 40–45. https://doi.org/10.1016/j.proeng.2014.11.261.

[28] Y. Pennec, J.O. Vasseur, B. Djafari-Rouhani, L. Dobrzyński, P.A. Deymier, Two-dimensional phononic crystals: Examples and applications, Surf. Sci. Rep. 65 (2010) 229–291. https://doi.org/10.1016/j.surfrep.2010.08.002.

[29] Y. Achaoui, A. Khelif, S. Benchabane, L. Robert, V. Laude, Experimental observation of locally-resonant and Bragg band gaps for surface guided waves in a phononic crystal of pillars, Phys. Rev. B. 83 (2011) 104201. https://doi.org/10.1103/PhysRevB.83.104201.

[30] E.P. Pokatilov, D.L. Nika, A.A. Balandin, Confined electron-confined phonon scattering rates in wurtzite AlN/GaN/AlN heterostructures, J. Appl. Phys. 95 (2004) 5626–5632. https://doi.org/10.1063/1.1710705.

[31] S. Uno, J. Hattori, K. Nakazato, N. Mori, Acoustic phonon modulation and electron-phonon interaction in semiconductor slabs and nanowires, J. Comput. Electron. 10 (2011) 104–120. https://doi.org/10.1007/s10825-010-0343-6.

[32] D.L. Nika, E.P. Pokatilov, A.A. Balandin, Phonon-engineered mobility enhancement in the acoustically mismatched silicon/diamond transistor channels, Appl. Phys. Lett. 93 (2008) 173111. https://doi.org/10.1063/1.3007986.

[33] V.A. Fonoberov, A.A. Balandin, Giant enhancement of the carrier mobility in silicon nanowires with diamond coating, Nano Lett. 6 (2006) 2442–2446. https://doi.org/10.1021/nl061554o.

[34] F.T. Vasko, V. V. Mitin, Generation and recombination processes via acoustic phonons in disordered graphene, Phys. Rev. B. 84 (2011) 155445. https://doi.org/10.1103/PhysRevB.84.155445.

[35] S. Alaie, D.F. Goettler, M. Su, Z.C. Leseman, C.M. Reinke, I. El-Kady, Thermal transport in phononic crystals and the observation of coherent phonon scattering at room temperature, Nat Commun. 6 (2015) 7228. http://dx.doi.org/10.1038/ncomms8228.

[36] E. Dechaumphai, R. Chen, Thermal transport in phononic crystals: The role of zone folding effect, J. Appl. Phys. 111 (2012) 073508. https://doi.org/10.1063/1.3699056.

[37] B.L. Davis, M.I. Hussein, Nanophononic metamaterial: Thermal conductivity reduction by local resonance, Phys. Rev. Lett. 112 (2014) 055505. https://doi.org/10.1103/PhysRevLett.112.055505.

[38] A. Haug, Phonon-assisted auger recombination in degenerate semiconductors, Solid State Commun. 22 (1977) 537–539. https://doi.org/10.1016/0038-1098(77)91409-0.

[39] I.A. Shojaei, S. Linser, G. Jnawali, N. Wickramasuriya, H.E. Jackson, L.M. Smith, F. Kargar, A.A. Balandin, X. Yuan, P. Caroff, H.H. Tan, C. Jagadish, Strong hot carrier effects in single nanowire heterostructures, Nano Lett. 19 (2019) 5062–5069. https://doi.org/10.1021/acs.nanolett.9b01345.

[40] K. Rostem, P.J. De Visser, E.J. Wollack, Enhanced quasiparticle lifetime in a superconductor by selective blocking of recombination phonons with a phononic crystal, Phys. Rev. B. 98 (2018) 014522. https://doi.org/10.1103/PhysRevB.98.014522.

[41] M. Lončar, T. Doll, J. Vučković, A. Scherer, Design and fabrication of silicon photonic crystal optical waveguides, J. Light. Technol. 18 (2000) 1402–1411. https://doi.org/10.1109/50.887192.

[42] V. V. Poborchii, T. Tada, T. Kanayama, Photonic-band-gap properties of two-dimensional lattices of Si nanopillars, J. Appl. Phys. 91 (2002) 3299–3305. https://doi.org/10.1063/1.1446659.

[43] N.A. Butakov, J.A. Schuller, Designing multipolar resonances in dielectric metamaterials, Sci. Rep. 6 (2016) 38487. https://doi.org/10.1038/srep38487.

[44] M. Garín, M. Solà, A. Julian, P. Ortega, Enabling silicon-on-silicon photonics with pedestalled Mie resonators, Nanoscale. 10 (2018) 14406–14413. https://doi.org/10.1039/c8nr02259c.

Chapter 2 Brillouin-Mandelstam Light Scattering

2.1 Introduction

Brillouin-Mandelstam spectroscopy (BMS) is an inelastic light scattering technique which measures the dispersion of the acoustic phonons and magnons in the energy range from 2 GHz to 900 GHz near the Brillouin zone (BZ) center. BMS is a nondestructive optical tool which has been widely used to probe acoustic phonons and magnons in various types of material systems including transparent amorphous and opaque materials [1–4], PnCs [5,6], nanospheres [7,8], membranes [9] and nanowires [10], ferromagnetic [11] and antiferromagnetic materials [12]. The principles of BMS are similar to those of Raman spectroscopy. Raman spectroscopy is used to observe optical phonons with energies of one or two orders of magnitudes higher than those of the acoustic phonons detectable with BMS. In this chapter, we will discuss the BMS experimental setup in back scattering configuration and explain different light scattering mechanisms which contribute to Brillouin scattering from different materials.

2.2 BMS Experimental Setup Configuration

BMS can be conducted in several optical configurations which have been explained in detail in the literature [13–15]. In this dissertation, we carried out BMS experiments in the backscattering geometry using a continuous wave (CW) solid state diode laser operating at the excitation wavelength $\lambda = 532\ nm$. A general schematic of the BMS spectroscopy in backscattering configuration is shown in Figure 2-1. The sample is placed on a translation stage with an incremental movement of ~1 μm. The laser light with vertical polarization of 1000:1 ratio passes a beam-splitter which divides it into two different optical paths. A small power (~0.1 to 0.5 mW) of the laser light is directed to the Fabry-Perot (FP) interferometer which is needed for the alignment purposes. The rest is transmitted to the collimator lenses (L1 and L2) in order to reduce the divergence of the beam. Then, using an iris the peripheral part of the laser beam is filtered out. The light is directed by the mirror M1 to the Glan-polarizer which increases the polarization ratio of the light to 100000:1. The half-wave plate after the Glan-polarizer selects the polarization (*p*- or *s*- polarization) of the incident light on the sample. The light hits a small mirror (M2) and focused on the sample using a lens (L3) with $f/\# = 1.4$. The angle of the incident light with respect to the normal to the sample is controlled from 15º to 70º using an automatic micro-rotational stage with an accuracy of 0.02º. This is required to select the phonon wave vector magnitude as described in the next sections. The in-plane orientation of the sample is also controllable using a small manual micro-rotational stage. The stage is required to select the crystallographic direction of the probing phonon wave vector. The scattered light from the sample is collected using

the same lens (L3) and focused and directed to the high resolution (3+3) pass tandem Fabry-Perot interferometer (JRS Instruments) via the lens (L4) and periscope system (M3 and M4). The multi-pass tandem FP interferometer consists of mirrors aligned and fixed parallel to each other at some distance spacing denoted by L_1 and L_2. In opaque materials, the elastically scattered light exceeds the intensity of the Brillouin component by more than a factor of 10^4-10^5. The tandem configuration is to increase the contrast and the finesse quality by increasing the cavity length and reducing the free-spectral range. The best arrangement of the spacing is fixing L_2 close to L_1 with ratio of 0.95. The details of the tandem FP instrument can be found elsewhere [1]. The transmitted light is detected by single-photon counter and analyzed using the special software.

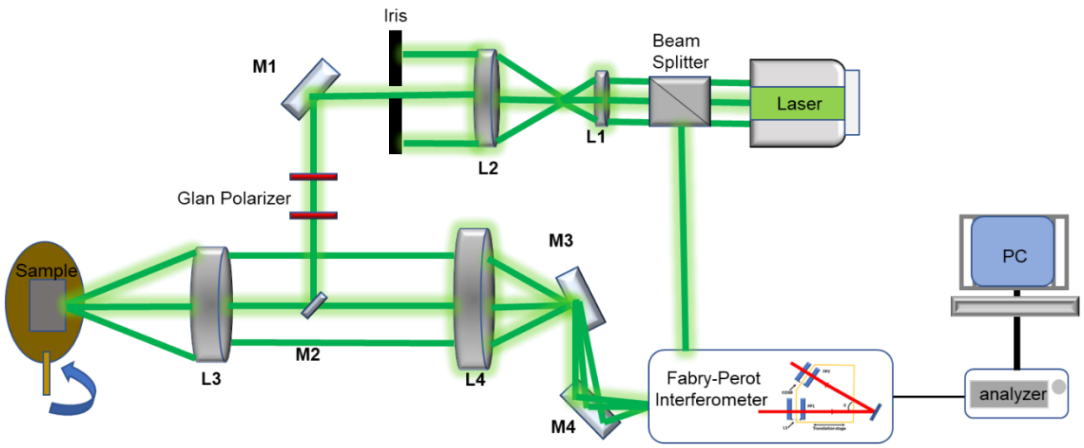

Figure 2-1: Schematic of the Brillouin-Mandelstam scattering setup in backscattering configuration. The rays represent the laser beam path and "M" and "L" indicate mirrors and lenses, respectively.

2.3 Light Scattering Mechanisms in Brillouin – Mandelstam Spectroscopy

In BMS, two different mechanisms contribute to light scattering. Their relative strength depends on the optical transparency of the material system at the wavelength of the excitation laser [1,2]. If the material system is optically transparent, scattering by the bulk of the material, involving "volumetric" phonons, is the dominant mechanism. If the material system is opaque or semi-transparent, the BMS spectrum is dominated by light scattering from the sample surface via the "ripple scattering" mechanism. In the latter case, only the in-plane component of the phonon momentum is conserved during the light scattering process. The magnitude of the in-plane component of the wave vector (or momentum) of the phonon participating in the scattering depends on the incident angle (θ) of the laser light with respect to the normal to the sample's surface. We will investigate the two aforementioned cases in detail in the succeeding sections.

2.3.1 Light Scattering by Bulk Phonons

Bulk phonons, or the volumetric phonons scatter light through the elasto-optic mechanism. Figure 2-2 (a) shows the scattering of light by bulk acoustic phonons with the wave vector ($\mathbf{q}$) and frequency (ω). As the incident light with wavelength λ_i and wave vector ($\mathbf{k_i}$) enters a medium with the refractive index of n, its wavelength and wave vector changes to $\lambda^* = \lambda/n$ and $k_i^* = 2\pi/\lambda^* = 2\pi n/\lambda$, respectively. The process of scattering of the light by bulk

phonons from the incident light $\mathbf{k_i^*}$, ω_i into the scattered state with wave vector $\mathbf{k_s^*}$ and ω_s must satisfy the conservation of momentum and energy equations which are expressed as follows [1]:

$$\mathbf{k_s^* - k_i^* = \pm q} \tag{2-1}$$

and,

$$\omega_s - \omega_i = \pm\omega \tag{2-2}$$

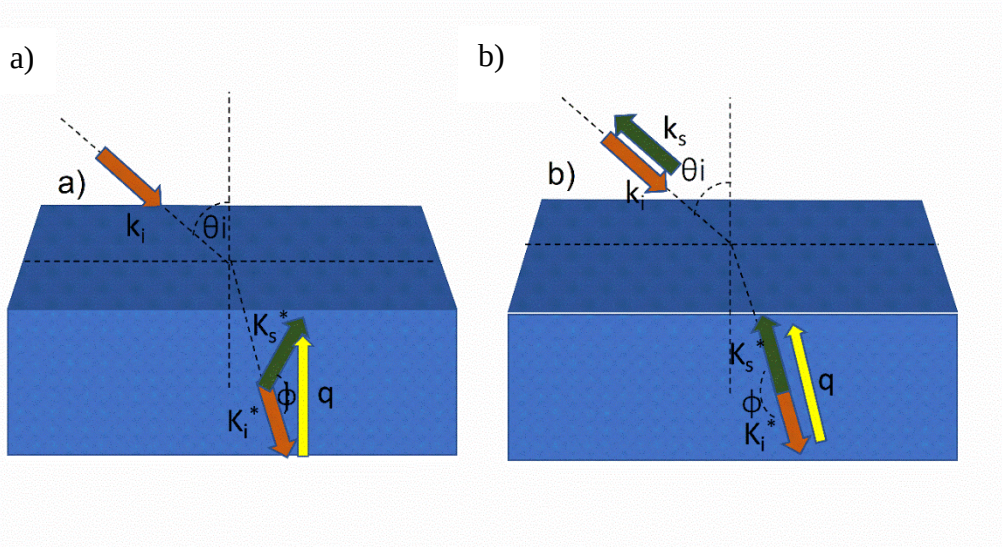

Figure 2-2: Schematic of BMS light scattering from bulk phonons. (a) The incident light is shown using the orange arrows while the scattered light is represented by the green arrows. The yellow arrow shows the acoustic phonon wave vector. The symbol ϕ is the scattering angle, which is different from the incident light angle θ_i. (b) The light scattering process in the backscattering configuration in which the scattering angle $\phi = 180°$.

In the process of light scattering, either the incident photon loses energy to generate a phonon (Stokes process) or gains energy by absorbing a phonon (anti-Stokes process). These two processes are expressed by "+" and "−" signs on the right hand side of equations (2-1) and (2-2), respectively. The change in the wave vector of the incident light during the scattering process covers a tiny portion of the BZ (about 10^8 cm^{-1}) close to BZ center (Γ) [2]. The dispersion of acoustic phonons close to BZ center is linear and thus, the angular frequency can be related to phonon wave vector as follows:

$$\omega(\mathbf{q}) = \upsilon|\mathbf{q}| \tag{2-3}$$

in which υ is the sound velocity in the material. Considering the scattering process depicted in Figure 2-2 (a) and considering equation (2-3), the energy conservation equation (2-2)can be stated as follows:

$$\frac{|\mathbf{k_s}| - |\mathbf{k_i}|}{n|\mathbf{q}|} = \frac{\upsilon}{c} \tag{2-4}$$

Sound travels at much slower velocities than that of the light. In fact, the order of magnitude of υ/c is ~10^{-5} and hence, we can assume that $|\mathbf{k_s}| \approx |\mathbf{k_i}| = k$ in which $k = 2\pi n/\lambda$. Therefore, the phonon wave vector probed by BMS is:

$$|\mathbf{q}| = \left(\frac{4\pi n}{\lambda}\right)\sin\left(\frac{\phi}{2}\right) \tag{2-5}$$

In this equation, ϕ is the scattering angle. In the backscattering configuration (Figure 2-2 (b)), the scattering angle $\phi = 180°$; therefore, the phonon wave vector **q** is defined as follows:

$$q = \frac{4\pi n}{\lambda} \tag{2-6}$$

As it is seen, in light scattering by bulk phonons in backscattering configuration, the magnitude of the phonon wave vector depends on refractive index of the material, n, and the excitation wavelength of the incident light, λ.

2.3.2 Light Scattering by Ripple Mechanism

High optical absorption in opaque materials induce uncertainties in determining the through-plane component of the phonon wave vector in the momentum conservation equation [1,2,16,17]. In these types of materials, only the in-plane component of the light scattering is conserved during the scattering process. In fact, in opaque and semi-transparent materials, thin films, metals, and PnCs scattering by ripple mechanism is the dominant source of the scattering [1,2]. In backscattering geometry, the in-plane

component of the phonon wave vector ($q_{\parallel}$) is conserved along the direction parallel to the surface of the sample. The incident, scattered, and the in-plane phonon wave vector is illustrated in Figure 2-3. Referring to this schematic, $q_{\parallel}$ can be obtained as follows:

$$q_{\parallel} = |\boldsymbol{k_i}| \sin\theta_i + |\boldsymbol{k_s}| \sin\theta_s \tag{2-7}$$

In backscattering geometry, $\theta_i = \theta_s = \theta$, the following expression can be stated as:

$$q_{\parallel} = 4\pi \sin\theta \,/\lambda \tag{2-8}$$

In scattering by ripple mechanism, one can see that $q_{\parallel}$ depends on the laser incident angle θ meaning that with variation of θ, one can select the $q_{\parallel}$ and thus obtain the dispersion of the phonons.

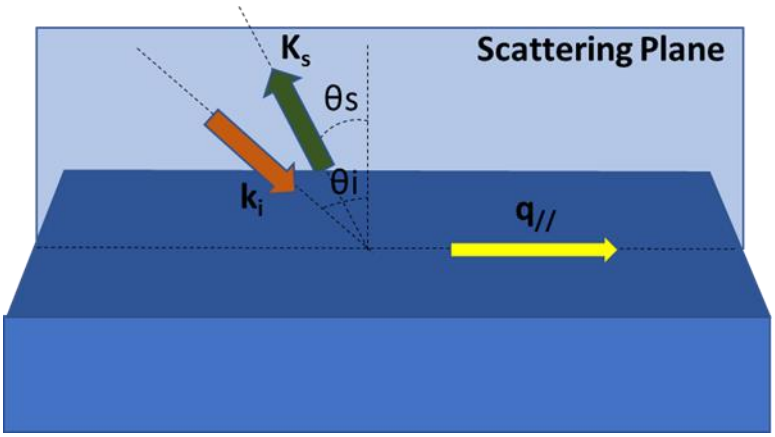

Figure 2-3: Illustration of the ripple scattering in the backscattering configuration. The phonon wave vector is parallel to the surface of the sample. In contrast to the scattering from bulk phonons, in ripple mechanism $q_{\parallel}$ wave vector can be varied by changing the incident angle.

2.4 Brillouin-Mandelstam Scattering on Transparent and Opaque Materials

BMS can be used to observe the acoustic phonons in liquids and solid crystalline and amorphous materials. Here, we present the results of our measurements of BMS on various material systems with different degrees of optical transparency. The experiments were intended to verify the BMS system performance and demonstrate its capability for a wide range of materials.

2.4.1 BMS of Crystalline Silicon Wafer

The BMS of crystalline silicon has been reported in the archival literature [17]. Due to the semitransparent nature of silicon at the excitation laser wavelength of $\lambda = 532$ nm, one would expect to observe both scattering from the bulk phonons and surface ripple mechanism. The BMS spectrum of the silicon (100) wafer is presented in Figure 2-4. The two peaks at 90.6 GHz and 135.3 GHz are attributed to the longitudinal (LA) and transverse (TA) acoustic phonons at $q = 0.0980\ \text{nm}^{-1}$. The volumetric phonon wave vector is calculated according to (2-5) knowing that the refractive index of silicon at $\lambda = 532$ nm is $n_1 = 4.15$ [18]. The LA and TA group phonon velocities (sound velocities) are calculated as $\upsilon_{LA} = \frac{2\pi f_{LA}}{q} = 8694\ \text{ms}^{-1}$and $\upsilon_{TA} = \frac{2\pi f_{TA}}{q} = 5802\ \text{ms}^{-1}$, respectively. The obtained results are in excellent agreement with previously reported data [17,19].

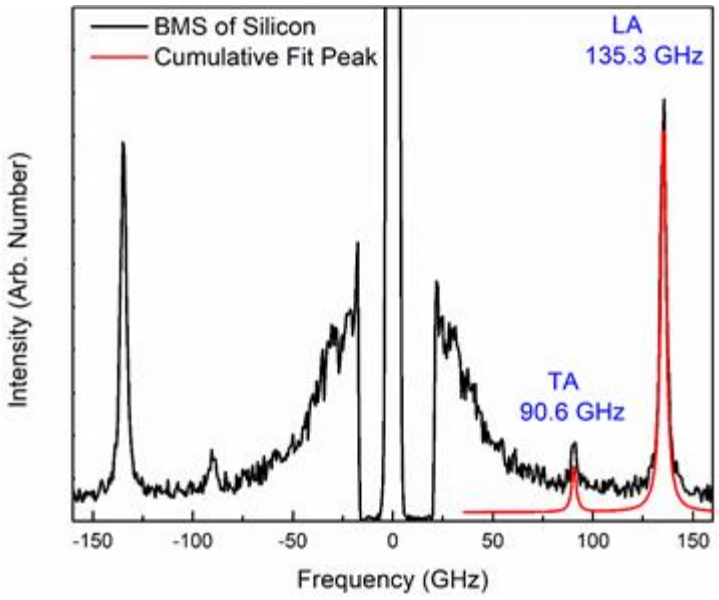

Figure 2-4: BMS data for bare silicon substrate. The spectrum shows two peaks attributed to the longitudinal (LA) and transverse (TA) acoustic phonons. The green and red curves are individual and cumulative Lorentzian fittings of the experimental data. The figure is adapted from Chun-Yu Huang et al., "Fine-tuning of the phonon spectrum and light – matter interactions in nanoscale pillar arrays," Nanoscale (in preparation, 2019).

BMS of the surface acoustic phonons in silicon at three different incident angles of $\theta = 40°, 50°, 60°$ associated with phonon wave vector of $q_{\parallel} = 15.2, 18.1, 20.5\ \mu m^{-1}$ are presented in Figure 2-5. Note that since the peaks are originated from the scattering of the light by surface ripple mechanism, the phonon wave vector should be calculated according to equation (2-8). The spectra show a very sharp peak at each laser incident angle which is attributed to the surface acoustic Rayleigh wave.

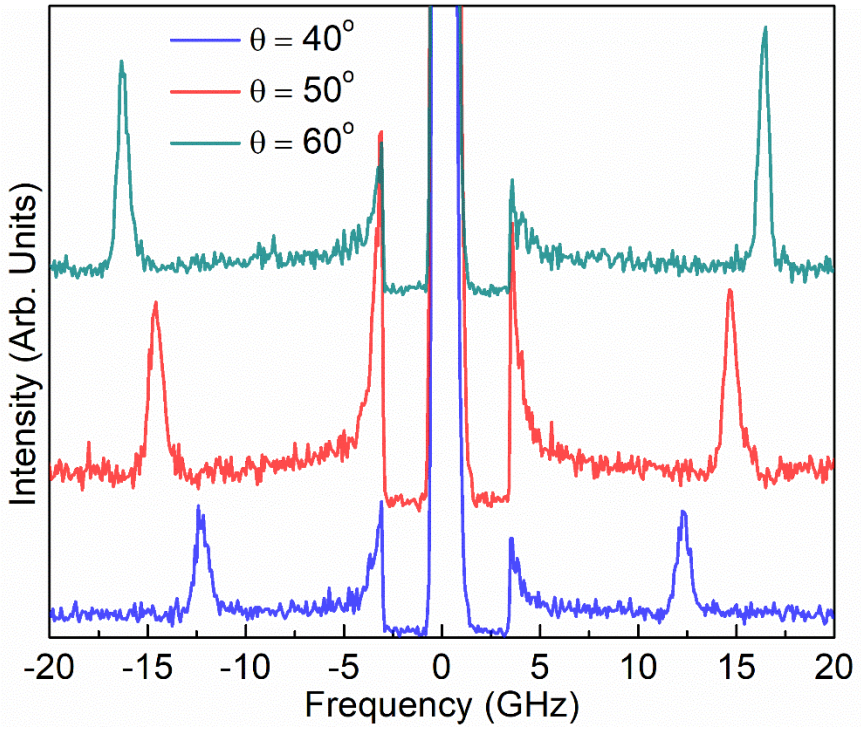

Figure 2-5: BMS data for bare silicon substrate at different laser incident angles. The spectrum shows one sharp peak at each accumulated spectrum attributed to the Rayleigh surface acoustic wave. The figure is adapted from Chun-Yu Huang et al., "Fine-tuning of the phonon spectrum and light – matter interactions in nanoscale pillar arrays," Nanoscale (in preparation, 2019).

2.4.2 BMS on Polymeric Materials: PVA and PVA with Single Wall Carbon Nanotube Composites

In the next set of experiments, we used Brillouin spectroscopy for the investigation of phonons in polyvinyl alcohol (PVA) polymer samples with different concentration of single wall carbon nanotubes (SWCNT). BMS has been widely used to detect the acoustic phonons and elastic coefficients in polymeric material systems [13–15,20–23]. Figure 2-6 (a) shows the optical images of the five different samples. The sample on the left is the

PVA without any fillers. As the concentration of the SWCNT increases, the sample becomes opaque. The samples are arranged from left to right as the filler concentration increases.

The BMS spectra of PVA with different SWCNT concentrations are shown in Figure 2-6 (b). The sharp peak observed in the BMS spectrum of the PVA film is attributed to the LA phonons. The phonon wave vector can be determined using Equation (2-6). With addition of SWCNT to PVA, the spectral position of the LA phonons shifts to lower frequencies. It should be noted that with incorporation of CNT fillers, the refractive index of the material changes as well. Therefore, in order to calculate the phonon group velocity ($\upsilon = \frac{\partial \omega}{\partial q}$) one should also acquire the refractive index as a function of filler concentration. Moreover, the full width at half maximum (FWHM) of the peaks increases as a result of adding fillers owing to the increase in the optical absorption at higher SWCNT concentrations. It should be noted that in BMS experiments for the opaque materials, the theoretical broadening follows $\Delta\omega = 2n_2/n_1$ where n_1 and n_2 are the real and imaginary parts of the complex refractive index of the material as $n = n_1 + in_2$.

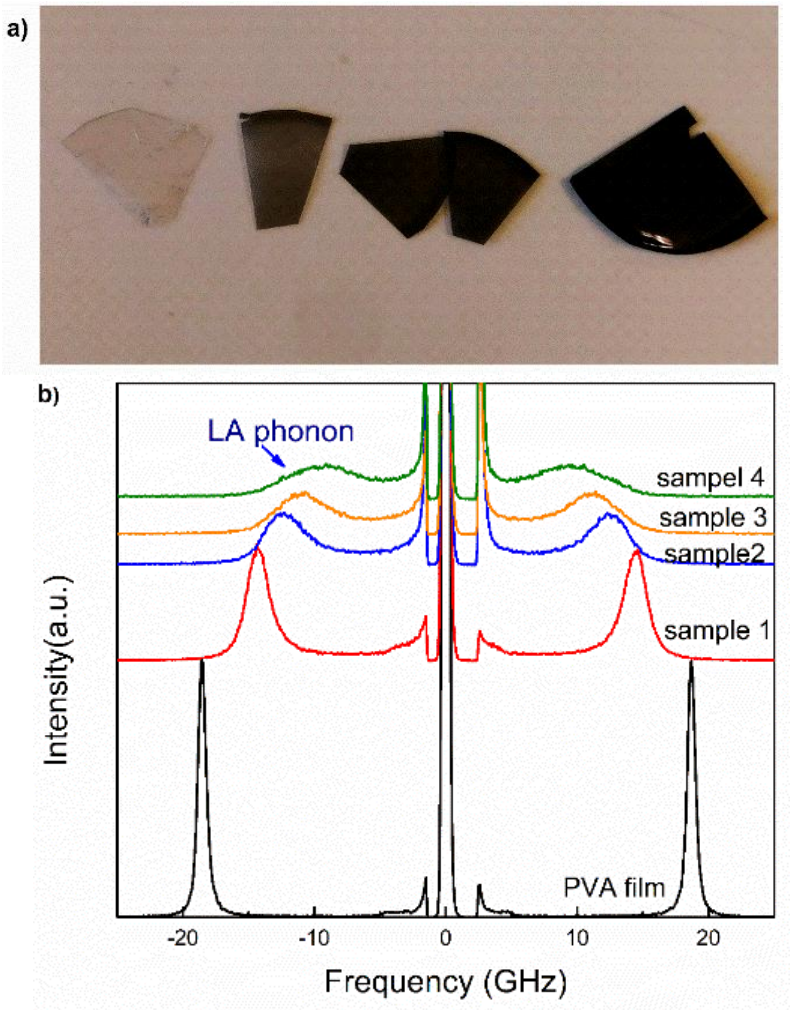

Figure 2-6: (a) Optical image of the PVA samples with different concentrations of SWCNT. b) BMS spectra of the samples accumulated in backscattering geometry. The increase in the filler concentration in the samples results in decreasing frequency of the peaks. The samples were provided by Professor Alex Rozhin Aston University, U.K.

2.4.3 BMS of Mineral Oil with Graphene Fillers

BMS can be used to extract the sound velocity liquids. Different mixtures of mineral oil with various concentrations of graphene are prepared and examined with BMS. Figure 2-7 (a-b) shows the optical images of the compounds and the accumulated data of pure mineral

oil and oil with graphene concentrations of $f = 2, 5, 7$ wt%. The peaks detected in all spectra are attributed to the volumetric longitudinal sound wave (LSW). As it is seen, the spectral position of LSW in mineral oil with $f = 2$ wt% of graphene is shifted to lower frequencies comparing to that of the pure mineral oil. With adding more graphene and at $f = 5$ wt% the frequency increases and at $f = 7$ wt% it decreases once again. Since the light is scattered from the volumetric longitudinal sound waves, the associated wave vector can be defined using equation (2-5) once the refractive indices of the compounds are measured.

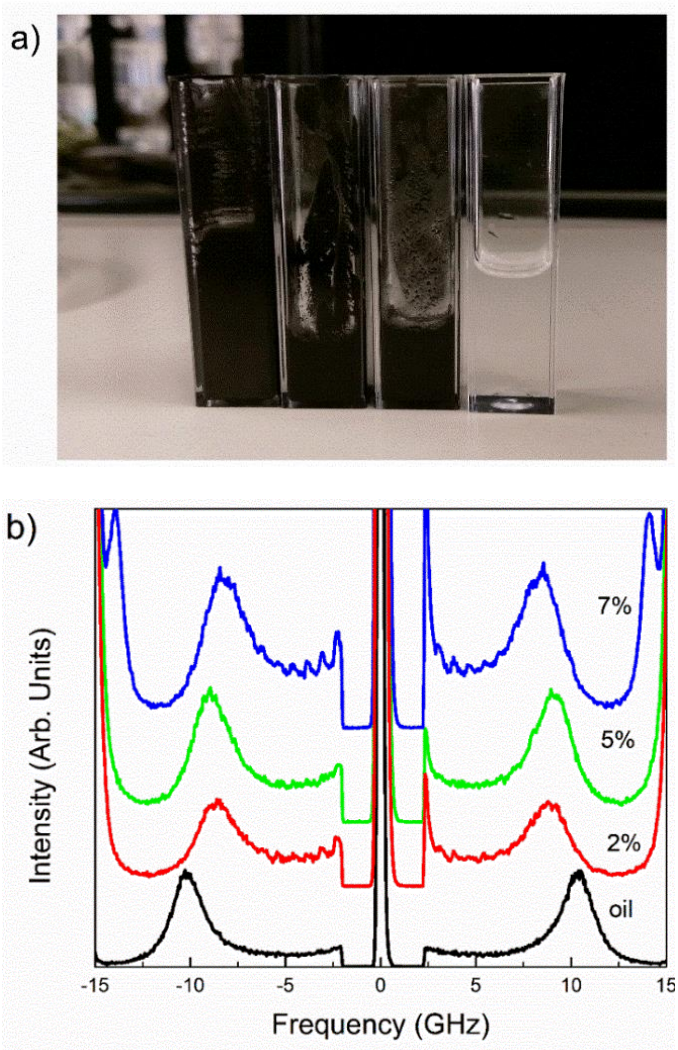

Figure 2-7: Thermal interface materials and Brillouin spectra. a) Mineral oil and the mixture of graphene and oil. b) Brillouin spectra of the samples with different graphene concentrations.

References:

[1] J.R. Sandercock, Trends in brillouin scattering: Studies of opaque materials, supported films, and central modes, Light Scatt. Solids III. 51 (1982) 173–206. https://doi.org/10.1007/3540115137_6.

[2] P. Mutti, C.E. Bottani, G. Ghislotti, M. Beghi, G.A.D. Briggs, J.R. Sandercock, Surface Brillouin scattering—Extending surface wave measurements to 20 GHz, in: A. Briggs (Ed.), Adv. Acoust. Microsc., Springer US, 1995: pp. 249–300. https://doi.org/10.1007/978-1-4615-1873-0_7.

[3] E. Alonso-Redondo, L. Belliard, K. Rolle, B. Graczykowski, W. Tremel, B. Djafari-Rouhani, G. Fytas, Robustness of elastic properties in polymer nanocomposite films examined over the full volume fraction range, Sci. Rep. 8 (2018) 16986. https://doi.org/10.1038/s41598-018-35335-1.

[4] F. Kargar, S. Ramirez, B. Debnath, H. Malekpour, R.K. Lake, A.A. Balandin, Acoustic phonon spectrum and thermal transport in nanoporous alumina arrays, Appl. Phys. Lett. 107 (2015) 171904. https://doi.org/10.1063/1.4934883.

[5] B. Graczykowski, M. Sledzinska, F. Alzina, J. Gomis-Bresco, J.S. Reparaz, M.R. Wagner, C.M. Sotomayor Torres, Phonon dispersion in hypersonic two-dimensional phononic crystal membranes, Phys. Rev. B. 91 (2015) 75414. https://doi.org/10.1103/PhysRevB.91.075414.

[6] D. Yudistira, A. Boes, B. Graczykowski, F. Alzina, L.Y. Yeo, C.M. Sotomayor Torres, A. Mitchell, Nanoscale pillar hypersonic surface phononic crystals, Phys. Rev. B. 94 (2016) 094304. https://doi.org/10.1103/PhysRevB.94.094304.

[7] T. Still, R. Sainidou, M. Retsch, U. Jonas, P. Spahn, G.P. Hellmann, G. Fytas, The “Music” of core−shell spheres and hollow capsules: Influence of the architecture on the mechanical properties at the nanoscale, Nano Lett. 8 (2008) 3194–3199. https://doi.org/10.1021/nl801500n.

[8] M.H. Kuok, H.S. Lim, S.C. Ng, N.N. Liu, Z.K. Wang, Brillouin study of the

quantization of acoustic modes in nanospheres, Phys. Rev. Lett. 90 (2003) 255502. https://doi.org/10.1103/PhysRevLett.90.255502

[9] J. Cuffe, E. Chávez, A. Shchepetov, P.-O. Chapuis, E.H. El Boudouti, F. Alzina, T. Kehoe, J. Gomis-Bresco, D. Dudek, Y. Pennec, B. Djafari-Rouhani, M. Prunnila, J. Ahopelto, C.M. Sotomayor Torres, Phonons in slow motion: Dispersion relations in ultrathin Si membranes, Nano Lett. 12 (2012) 3569–3573. https://doi.org/10.1021/nl301204u.

[10] F. Kargar, B. Debnath, J.-P. Kakko, A. Saÿätjoki, H. Lipsanen, D.L. Nika, R.K. Lake, A.A. Balandin, Direct observation of confined acoustic phonon polarization branches in free-standing semiconductor nanowires, Nat. Commun. 7 (2016) 13400. https://doi.org/10.1038/ncomms13400.

[11] B. Hillebrands, C. Mathieu, M. Bauer, S.O. Demokritov, B. Bartenlian, C. Chappert, D. Decanini, F. Rousseaux, F. Carcenac, Brillouin light scattering investigations of structured permalloy films, J. Appl. Phys. 81 (1997) 4993–4995. https://doi.org/10.1063/1.364881.

[12] M.M. Lacerda, F. Kargar, E. Aytan, R. Samnakay, B. Debnath, J.X. Li, A. Khitun, R.K. Lake, J. Shi, A.A. Balandin, Variable-temperature inelastic light scattering spectroscopy of nickel oxide: Disentangling phonons and magnons, Appl. Phys. Lett. 110 (2017) 202406. https://doi.org/10.1063/1.4983810.

[13] J.K. Krüger, A. Marx, L. Peetz, R. Roberts, H.G. Unruh, Simultaneous determination of elastic and optical properties of polymers by high performance Brillouin spectroscopy using different scattering geometries, Colloid Polym. Sci. 264 (1986) 403–414. https://doi.org/10.1007/BF01419544.

[14] J.K. Krüger, J. Embs, J. Brierley, R. Jiménez, A new Brillouin scattering technique for the investigation of acoustic and opto-acoustic properties: Application to polymers, J. Phys. D. Appl. Phys. 31 (1998) 1913–1917. https://doi.org/10.1088/0022-3727/31/15/021.

[15] J. Krüger, L. Peetz, M. Pietralla, Brillouin scattering of semicrystalline poly(4-methyl-1-pentene): study of surface effects of bulk and film material, Polymer

(Guildf). 19 (1978) 1397–1404. https://doi.org/10.1016/0032-3861(78)90091-5.

[16] J.R. Sanderocock, Light scattering from surface acoustic phonons in metals and semiconductors, Solid State Commun. 26 (1978) 547–551. https://doi.org/http://dx.doi.org/10.1016/0038-1098(78)91307-8.

[17] J.R. Sandercock, Brillouin-scattering measurements on silicon and germanium, Phys. Rev. Lett. 28 (1972) 237–240. https://doi.org/10.1103/PhysRevLett.28.237.

[18] D.E. Aspnes, A.A. Studna, Dielectric functions and optical parameters of Si, Ge, GaP, GaAs, GaSb, InP, InAs, and InSb from 1.5 to 6.0 eV, Phys. Rev. B. 27 (1983) 985–1009. https://doi.org/10.1103/PhysRevB.27.985.

[19] K.S. Olsson, N. Klimovich, K. An, S. Sullivan, A. Weathers, L. Shi, X. Li, Temperature dependence of Brillouin light scattering spectra of acoustic phonons in silicon, Appl. Phys. Lett. 106 (2015) 51906. https://doi.org/10.1063/1.4907616.

[20] J. Krüger, K. Bohn, J. Schreiber, Anomalous behavior of the longitudinal mode Grüneisen parameter around the glass transition as revealed by Brillouin spectroscopy: Polyvinylacetate, Phys. Rev. B - Condens. Matter Mater. Phys. 54 (1996) 15767–15772. https://doi.org/10.1103/PhysRevB.54.15767.

[21] B. Graczykowski, A. Gueddida, B. Djafari-Rouhani, H.J. Butt, G. Fytas, Brillouin light scattering under one-dimensional confinement: Symmetry and interference self-canceling, Phys. Rev. B. 99 (2019) 165431. https://doi.org/10.1103/PhysRevB.99.165431.

[22] M. Hesami, A. Gueddida, N. Gomopoulos, H.S. Dehsari, K. Asadi, S. Rudykh, H.J. Butt, B. Djafari-Rouhani, G. Fytas, Elastic wave propagation in smooth and wrinkled stratified polymer films, Nanotechnology. 30 (2019) 045709. https://doi.org/10.1088/1361-6528/aaee9b.

[23] E.M. Brody, C.J. Lubell, C.L. Beatty, Measurement of the Grüneisen number in polystyrene by brillouin light scattering, J. Polym. Sci. Polym. Phys. Ed. 13 (1975) 295–301. https://doi.org/10.1002/pol.1975.180130207.

[24] M. Nomura, Y. Kage, D. Müller, D. Moser, O. Paul, Electrical and thermal properties of polycrystalline Si thin films with phononic crystal nanopatterning for thermoelectric applications, Appl. Phys. Lett. (2015). https://doi.org/10.1063/1.4922198.

[25] Q. Liang, Y.L. He, Q. Ren, Y.P. Zhou, T. Xie, A detailed study on phonon transport in thin silicon membranes with phononic crystal nanostructures, Appl. Energy. 227 (2018). https://doi.org/10.1016/j.apenergy.2017.07.083.

[26] F. Kargar, E.H. Penilla, E. Aytan, J.S. Lewis, J.E. Garay, A.A. Balandin, Acoustic phonon dispersion engineering in bulk crystals via incorporation of dopant atoms, Appl. Phys. Lett. 112 (2018) 191902. https://doi.org/10.1063/1.5030558.

Chapter 3 Nanofabrication of Phoxonic Crystals

3.1 Introduction

This chapter focuses on the techniques, processes, and tools required for the fabrication of different types of PnC structures including air-hole and pillar arrays with different diameters and periodicity. At the end of this chapter, the step-by-step fabrication procedure of the specially designed "pillar with the hat" structure is described in detail.

3.2 Fabrication Methods

A lithographic approach is usually used to pattern a photoresist using electron beam lithography (EBL) and focused ion beam (FIB) direct writing. EBL can provide high resolution due to the short wavelength which ranges from 10 keV to 50 keV and can pattern complex structures. An example of the pattern used in this study is shown in Figure 3-1. In EBL, drift in exposure dose can cause inhomogeneities across the patterned sample. Hence, proper dosage and test monitoring are required. The EBL and FIB systems used in this study are shown in Figure 3-2 (a-b). The flowchart of the step-by-step fabrication procedure via EBL is presented in Figure 3-3.

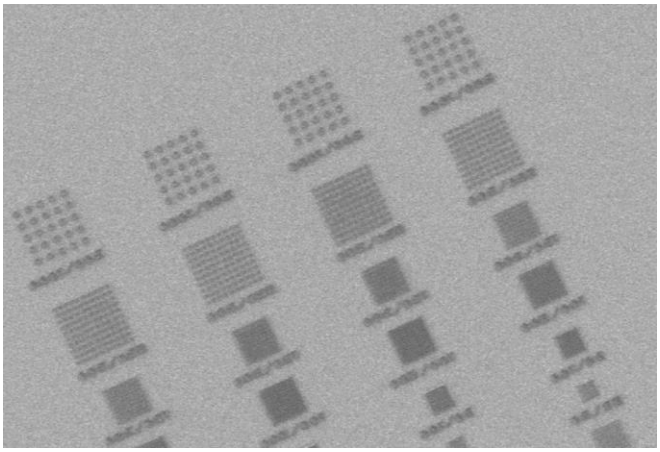

Figure 3-1: Scanning electron microscopy (SEM) of the pattern with different diameters and pitches used for making phononic crystal arrays

(a)

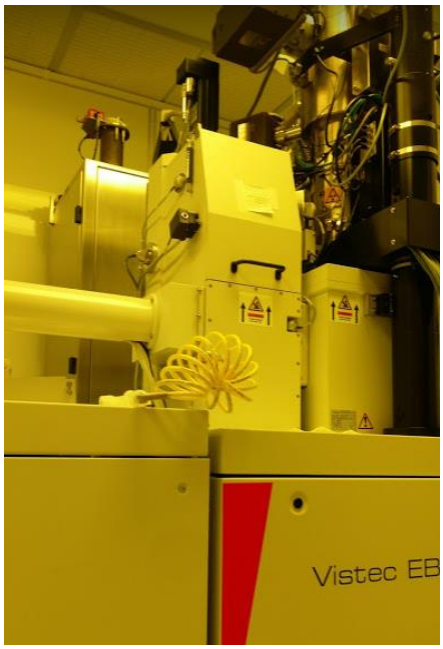

(b)

Figure 3-2: (a) Electron beam lithography and (b) Focused ion beam and scanning electron microscopy systems used for fabrication of the samples.

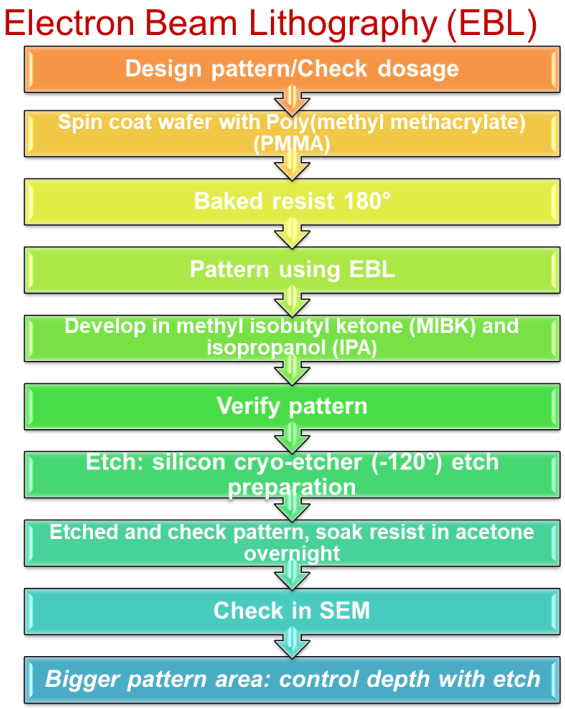

Figure 3-3: The flowchart of the step-by-step nanofabrication processes using electron beam lithography.

FIB can also be used in order to design the PnCs. However, it is more difficult to utilize FIB in order to fabricate nanosized structures since one must use low beam current for the small spot size and resolution. Comparing the FIB method, EBL is still the most convenient way of nanofabrication [3–6]. The step-by-step flowchart of FIB application for PnC structures is illustrated in Figure 3-4.

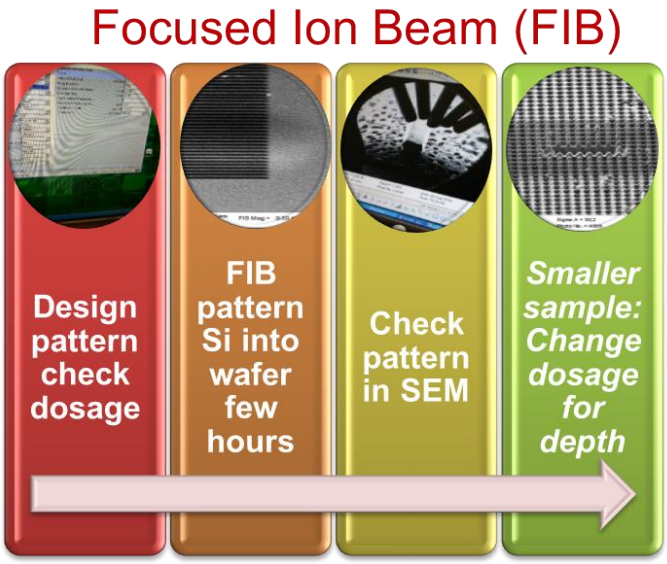

Figure 3-4: The flowchart of the step-by-step nanofabrication procedure using FIB.

3.3 Different Shape of Phononic Crystal Structures

PnCs are an array of air holes or pillars arranged in specific lattice configurations. The dimensions of the holes and the periodicity define the phonon frequency range to be engineered. Typically, in order to modify the phonon dispersion in GHz frequency range, one needs to fabricate structures with characteristic size of few tens to hundreds of nanometers. A set of phononic crystals with air-hole and pillar structures arranged in square lattice fabricated with electron beam lithography is shown in Figure 3-5. The diameter of the holes varies from 100 nm to 1μm and the spacing between them is in the range of 50 nm to 500 nm. Several parameters in designing of the one-dimensional (1-D) and two-dimensional (2D) PnCs from fabrication perspectives including the height of the pillars, h,

the pitch of the arrays, a; and the diameter of the air holes, d, have ben examined. The fabrication process is introduced in the following text.

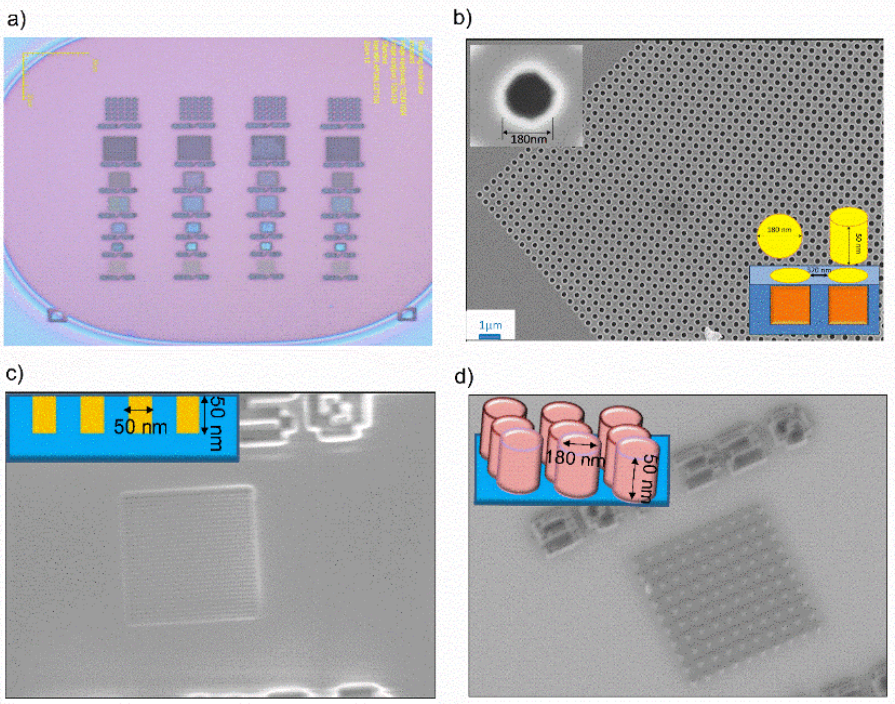

Figure 3-5: Optical and scanning electron microscopy images. (a) Optical microscopy image of the air hole pattern and SEM images of (b) the hole array, (c) the poly (methyl methacrylate) hole array of 400×400 μm and (d) the poly (methyl methacrylate) pillar array.

3.3.1 Fabrication of 1-D PnCs

1-D PnCs are structures consists of periodic layers of materials or grooves with specific thicknesses and spacings in one dimension. Previous studies reported the surface longitudinal resonance (LR) modes and folding of pure Rayleigh surface acoustic waves (RW) and an interaction between them using BMS in 1-D PnCs [5]. Another example is the free silicon surface in the form of periodic stripes led to the existence of different

dispersive surface acoustic waves (SAW) propagating along the strips and grooves [15,16]. We used FIB to fabricate a 1-D PnC structure on the silicon (100) wafer with grooves 60 nm and periodicity of 300 nm. The characteristic parameters of the 1-D PnC were examined and modified several times. The fabricated final structure is shown in Figure 3-6. As previously stated, it is rather hard to control the depth of the trench using FIB method. We estimated the approximate depth of the grooves to be less than 100 nm. The total sample size is about 300 by 300 µm.

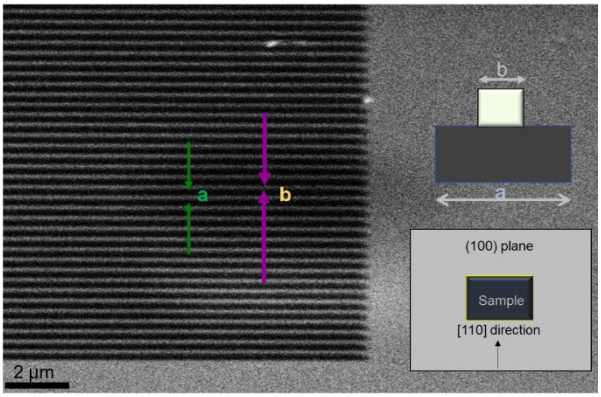

Figure 3-6: Focused ion beam pattern of 1-D grooves. A schematic of the sample shape and direction on silicon (100) substrate with the periodicity a = 300 nm and b = 60 nm.

3.3.2 Fabrication of 2-D PnCs

Similar to 1-D PnCs, the 2-D PnCs are consisted of air-holes or pillars arranged in a specific lattice configuration fabricated on a surface of a material. In our study, several 2-D PnC structures were fabricated in a square lattice with different hole and pillar characteristic dimensions on a (100) silicon substrate. After examining many tunable parameters, we

fabricated the “pillar with hat” structures on a silicon (100) orientation wafer cut into direction <110>. The pillars were arranged in the square lattice. The general schematic of fabrication procedure of the 2-D PnCs is shown in Figure 3-7. Here is the list of steps that we followed for fabrication of our structures. Our method is a slightly different variation of the methodology followed by other groups A similar [8–11].

I. ***Deposition of photoresist layer:*** A thin film of 950 A2 Poly (methyl methacrylate) (PMMA) was dispensed on the silicon chips using a spin coating method at 4000 rpm. The approximate thickness of the layer created by this method is 200 nm.

II. ***Curing of PMMA film:*** The chip was baked for 1 minute at 170 °C above the glassy temperature of PMMA. This results in a solid shiny layer of PMMA on top of the silicon wafer.

III. ***Patterning with EBL:*** The structure of the PnC was patterned using electron beam lithography (EBL). PMMA breaks down into monomers upon exposure of electrons. The exposed regions were rinsed away (developed) using in a methyl isobutyl ketone: isopropanol solution (1:3).

IV. ***Etching:*** After the development step, the chip consists of a layer of patterned PMMA thin film on top. The silicon is etched away using the Silicon Trench Etch system (Oxford Cobra Plasmalab Model 100) (Figure 3-8) at -120 °C. This is required to slow down the etch rate. The flow of the SF_6 at certain flow rates results in air-hole or pillar based PnCs.

V. ***PMMA lift-off:*** The PMMA resist layer was washed away by leaving the sample in acetone for 24 hours.

VI. ***SEM characterization:*** In the end, the samples should be carefully characterized by SEM. Different SEM images from various angles of views are required to determine the characteristic dimensions of the PnC structures.

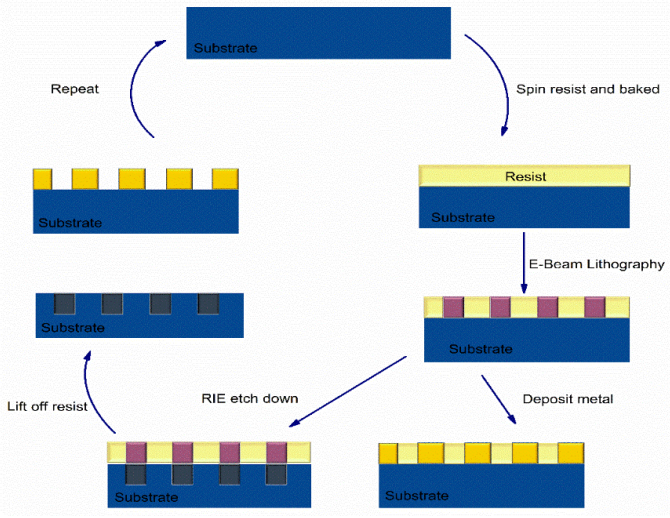

Figure 3-7: Schematic of the step-by-step fabrication procedure of air hole and pillar-based PnC structures.

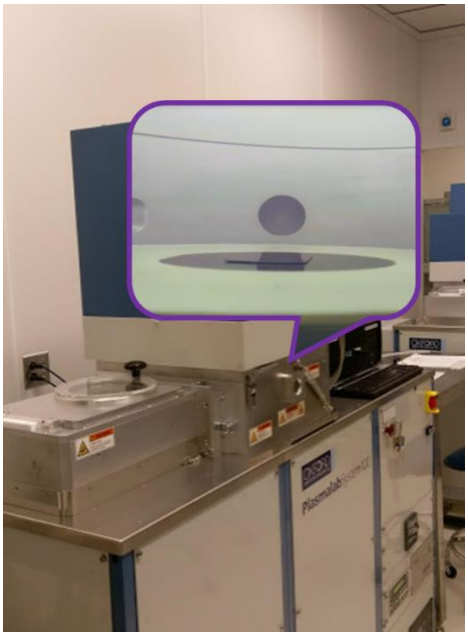

Figure 3-8: Silicon trench etch system used for etching the silicon pillars.

References:

[1] D.R. Brambley, Electron-beam technology in microelectronic fabrication, IEE Proc. I Solid State Electron Devices. (1982). https://doi.org/10.1049/ip-i-1.1982.0007.

[2] M.A. Mohammad, M. Muhammad, S.K. Dew, M. Stepanova, Fundamentals of electron beam exposure and development, in: Nanofabrication Tech. Princ., 2012. https://doi.org/10.1007/978-3-7091-0424-8_2.

[3] A. Sarangan, Nanofabrication, in: Fundam. Appl. Nanophotonics, 2016. https://doi.org/10.1016/B978-1-78242-464-2.00005-1.

[4] A.A. Tseng, K. Chen, C.D. Chen, K.J. Ma, Electron beam lithography in nanoscale fabrication: Recent development, IEEE Trans. Electron. Packag. Manuf. (2003). https://doi.org/10.1109/TEPM.2003.817714.

[5] J.R. Dutcher, S. Lee, B. Hillebrands, G.J. McLaughlin, B.G. Nickel, G.I. Stegeman, Surface-grating-induced zone folding and hybridization of surface acoustic modes, Phys. Rev. Lett. 68 (1992) 2464–2467. http://link.aps.org/doi/10.1103/PhysRevLett.68.2464.

[6] B. Graczykowski, M. Sledzinska, N. Kehagias, F. Alzina, J.S. Reparaz, C.M. Sotomayor Torres, C.M.S. Torres, Hypersonic phonon propagation in one-dimensional surface phononic crystal, Appl. Phys. Lett. 104 (2014) 1–5. https://doi.org/10.1063/1.4870045.

[7] P.G. Domadiya, E. Manconi, M. Vanali, L. V. Andersen, A. Ricci, Numerical and experimental investigation of stop-bands in finite and infinite periodic one-dimensional structures, JVC/Journal Vib. Control. 22 (2016). https://doi.org/10.1177/1077546314537863.

[8] R. Zhang, J. Sun, Design of silicon phoxonic crystal waveguides for slow light enhanced forward stimulated brillouin scattering, J. Light. Technol. 35 (2017) 2917–2925. https://doi.org/10.1109/JLT.2017.2704615.

[9] J. Lou, L. He, J. Yang, S. Kitipornchai, H. Wu, Wave propagation in viscoelastic phononic crystal rods with internal resonators, Appl. Acoust. 141 (2018). https://doi.org/10.1016/j.apacoust.2018.07.029.

[10] E. Alonso-Redondo, H. Huesmann, E.H. El Boudouti, W. Tremel, B. Djafari-Rouhani, H.J. Butt, G. Fytas, Phoxonic hybrid superlattice, ACS Appl. Mater. Interfaces. 7 (2015) 12488–12495. https://doi.org/10.1021/acsami.5b01247.

[11] L.C. Parsons, G.T. Andrews, Off-axis phonon and photon propagation in porous silicon superlattices studied by Brillouin spectroscopy and optical reflectance, J. Appl. Phys. 116 (2014) 033510. https://doi.org/10.1063/1.4890319.

Chapter 4 Phononic and Photonic Properties of Nanopillars with Hats

4.1 Introduction

In this chapter, the results of the BMS experiments and variable angle spectroscopic ellipsometry (VASE) of the silicon "pillar with hat" structures are presented. BMS results clearly show that phonon dispersion in these structures are modified significantly. The experimental data has been analyzed carefully and compared to the finite element method (FEM) simulations. The VASE results suggest that these structures also act as photonic crystals.

4.2 Sample Fabrication and Characterization

In Figure 4-1 (a-b) we present a schematic of the silicon "pillar with hat" PxCs on a 500-μm thick silicon substrate with the associated dimensions and substrate crystallographic directions. The 500-nm tall pillars are arranged in a square lattice on a 1 mm × 1 mm (100) silicon chip along the <110> crystallographic directions with the inter-pillar center-to-center distance of $d = 500$ nm. The base of the silicon pillars is slightly larger than its end where it connects to the "hat" structure. The "hat" structure on top of the pillars has a

symmetric shape with 443-nm lateral dimension (Figure 4-1-b). The unit cell of the PxC contains a quarter of each pillar with the space between them. Figure 4-1 (c-f) illustrates the step-by-step fabrication procedure of the PxCs. A thin layer of photoresist poly (methyl methacrylate) (PMMA 950 A2) was spin-deposited on a 500 μm thick (100) orientation silicon wafer and patterned in a square lattice arrays in the desired dimensions using the electron beam lithography (Figure 4-1-c). The silicon was then etched away using the silicon trench etch system (Oxford Cobra Plasmalab Model 100) at -120 ºC under SF_6 and O_2 gas flow at 80 SCCM and 18 SCCM, respectively. Etching at low temperatures is required to slow down and control the process so that the structure will acquire the designer "pillar with hat" geometry. The arrangement of the pillars on the silicon wafer and the related crystallographic directions are shown in Figure 4-2.

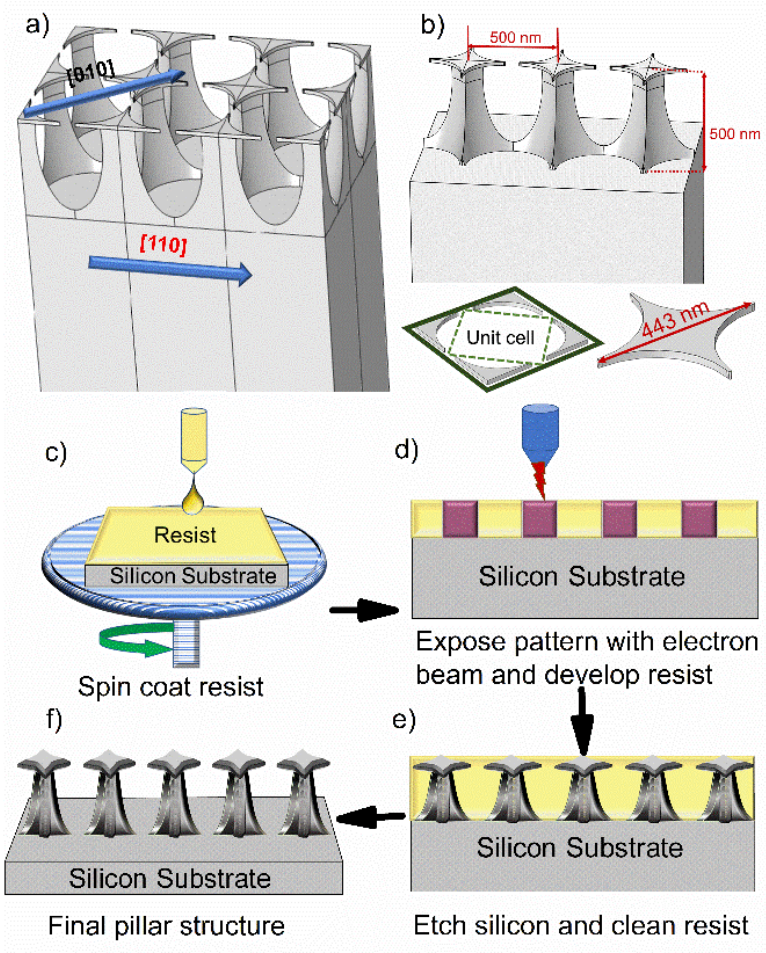

Figure 4-1: Schematic of the "pillars with hat" structures on silicon substrate, showing (a) the crystallographic directions and the square lattice configuration, and (b) the geometry and features sizes of the nano-pillars. The periodic lattice consists of nano-pillars with 500-nm height and 500-nm pitch. The pillars have a symmetric "hat like" structure on top, which provides additional tunability for the phononic – photonic crystals. (c-f) Step-by-step illustration of the fabrication procedure. The figure is adapted from Chun-Yu Huang et al., "Fine-tuning of the phonon spectrum and light – matter interactions in nanoscale pillar arrays," Nanoscale (in preparation, 2019).

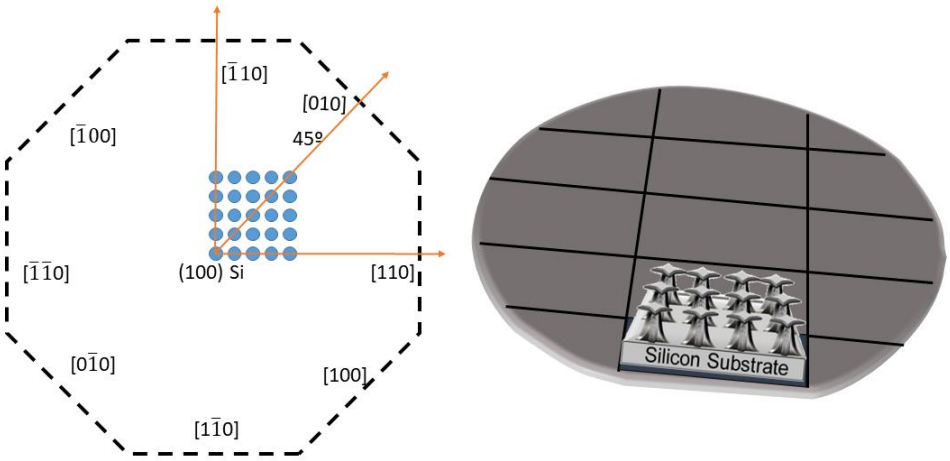

Figure 4-2: The crystallographic directions of the Si wafer used in this study. The arrays of pillars are fabricated in a square lattice along <110> directions. The BMS have been conducted with phonon wave vector$q_{\parallel}$ along [110] and [010] directions. The figure is adapted from Chun-Yu Huang et al., "Fine-tuning of the phonon spectrum and light – matter interactions in nanoscale pillar arrays," Nanoscale (in preparation, 2019).

The obtained samples were characterized using the scanning electron microscopy (SEM) (Figure 4-3 (a-d)). It may appear from the side view of the SEM image shown in Figure 4-3 (a) that the adjacent pillars are connected to each other via their "hats". However, a magnified image of the pillars from the front and top views and at tilted angles presented in Figure 4-3 (b-d) confirms that the nanostructures are completely separated as desired. The illusion of connected "hats" originates from the optical effects at low magnification and a certain angle of view.

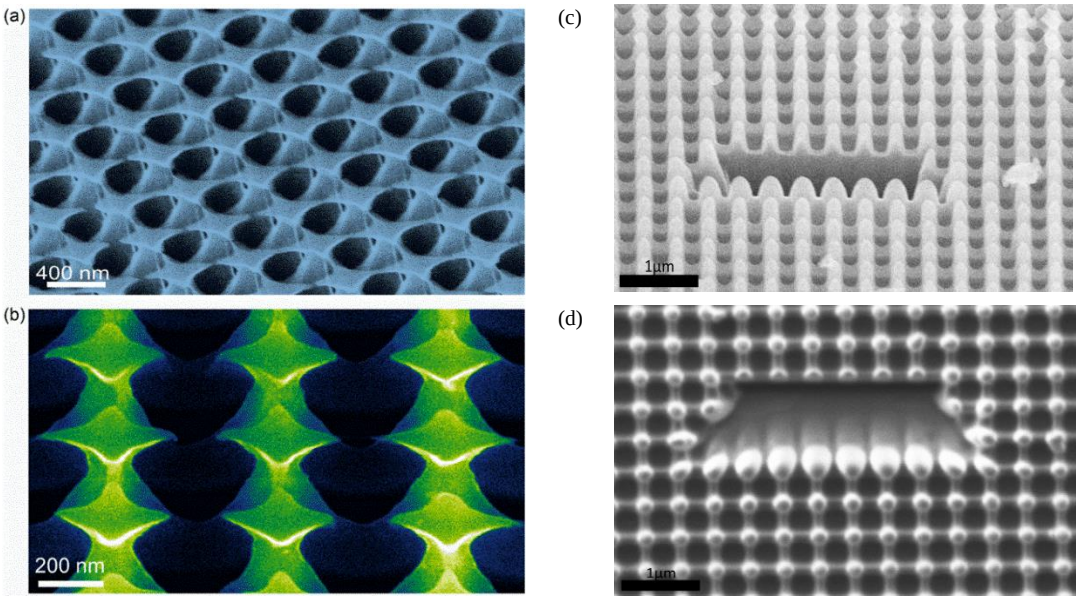

Figure 4-3: SEM images of (a) the side view and (b) front view of the arrays and individual pillar structure. (c) SEM image of the pillars at a tilted angle. The cut has been created intentionally by FIB milling in order to accurately measure the height of the pillars at the tilted angle. (d) Top-view of the area of the cut and the pillars. The figure is adapted from Chun-Yu Huang et al., "Fine-tuning of the phonon spectrum and light – matter interactions in nanoscale pillar arrays," Nanoscale (in preparation, 2019).

4.3 Results

4.3.1 BMS Spectra of "Pillar with Hat"

BMS experiments were carried out in the backscattering geometry using a continuous wave (CW) solid state diode laser operating at the excitation wavelength $\lambda = 532\,nm$. The incident light was *p*-polarized while there was no polarization selection for the scattered light. The laser light was focused on the sample using a lens with $f/\# = 1.4$. The angle of the incident light with respect to the normal to the sample has been changed from 16º to

52º using an automatic micro-rotational stage with an accuracy of 0.02º. This is required to select the phonon wave vector magnitude as described in the manuscript. The orientation of the sample has been adjusted using a small manual micro-rotational stage. The stage is required to select the crystallographic direction of the probing phonon wave vector. The scattered light from the sample was collected using the same lens and directed to the high resolution (3+3) pass Fabry-Perot interferometer (JRS Instruments).

Figure 4-4 (a) shows BMS data for the "pillar with hats" at $\theta = 50°$ corresponding to the phonon wave vector of $q_{\parallel} = 18.1\ \mu m^{-1}$ along the [110] crystallographic direction. All of the observed peaks are fitted using individual Lorentzian functions. The peaks at higher frequencies exhibit a rather large full width at half maximum (FWHM) when fitted with only one Lorentzian function. However, these broad peaks consist of two or more individual phonon peaks with frequencies too close to each other to resolve visually. In these cases, the peak deconvolution with several Lorentzian functions has been utilized. As one can see, there are nine peaks, including the peak shown in the inset, attributed to different phonon polarization branches. The peaks appear in the frequency range from 2 GHz to 20 GHz as a result of nanostructuring. The intensity of the peak at 2.2 GHz is higher than that of the rest of the peaks. For this reason, it has been plotted separately as an inset.

In Figure 4-4 (b), we present the evolution of the phonon peaks for the "pillar with hats" structure as a function of $q_{\parallel}$ varied by changing the incident light angle in the range of $28° < \theta < 52°$. This angle range corresponds to the phonon wave vectors range of $11.1\ \mu m^{-1} \leq q_{\parallel} \leq 18.6\ \mu m^{-1}$. All of the peaks observed in Figure 4-4 (a) are present in

the spectra accumulated at different $q_{\parallel}$ with almost no observable changes in their spectral position, demonstrating that the frequency of the phonons does not depend on the phonon wave vector. This is an indication of the localized or standing phonon modes either within the "pillar with hats" structure or in the substrate space between the pillars as a result of Bragg's condition. The localized phonon modes possess zero group velocity ($v_g = \frac{\partial \omega}{\partial q} \sim 0$) and are hybrid in nature, revealing a complicated vibration displacement profile. The intensity of the peaks, however, changes for the different $q_{\parallel}$. For a semi-infinite opaque material, with the light scattering by surface ripple mechanism in the backscattering geometry, the total power, dP, scattered into the solid angle, $d\Omega$, for the light with polarization in the scattering plane, is described as $\frac{1}{P}\left(\frac{dP}{d\Omega}\right) = \frac{\omega_s^4}{\pi^2 c^4} A cos^4(\theta) R(\theta) \overline{e_z(0)^2}$ [1,15]. Here ω_s is the frequency of the scattered light, c is the speed of light in vacuum, A is the area of the sample under illumination, $R(\theta)$ is the surface reflectivity which is by itself a function of the incident light angle θ, and $\overline{e_z(0)^2}$ is the mean square displacement of the surface at sample's interface. As one can see, the intensity of the scattered light for a specific phonon polarization branch depends on the reflectivity at the incident angle of θ, which now also depends on the orientation and geometry of the pillars. These modes are very different from the bulk LA and TA phonons. The true bulk LA and TA phonons of silicon reveal two peaks at 90.6 GHz and 135.3 GHz as shown in Figure 2-4.

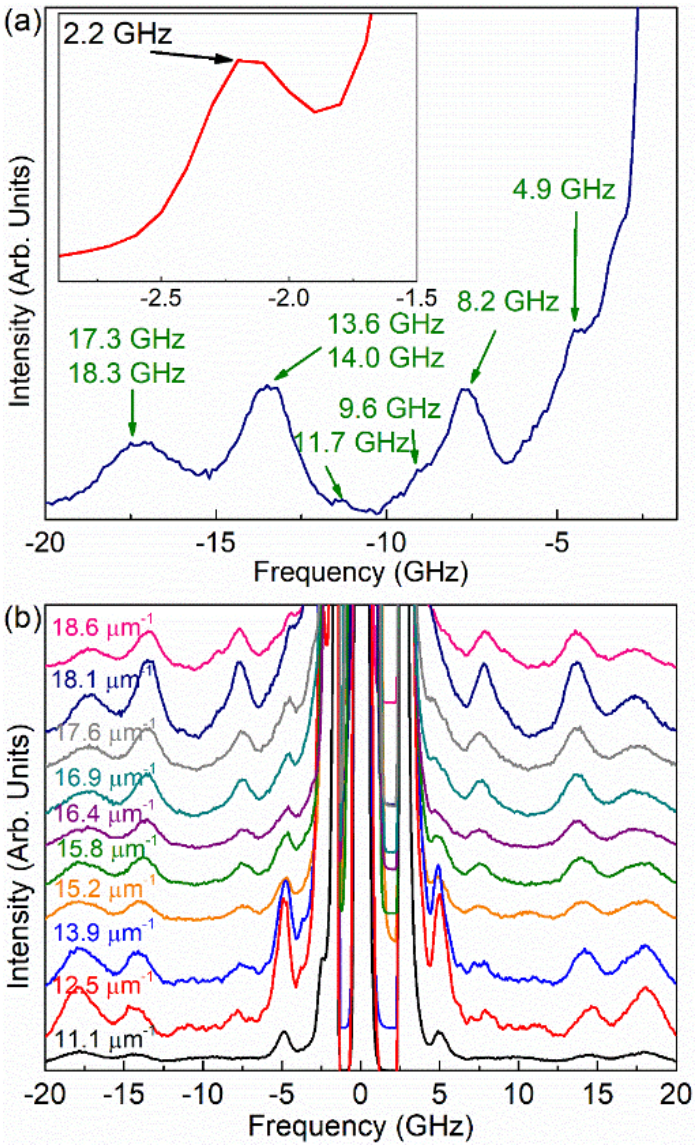

Figure 4-4: Brillouin-Mandelstam spectroscopy data for (a) the "pillar with hat" structures accumulated at the incident light angle of 50°, corresponding to the in-plane phonon wave vector of $q_{\parallel} = 18.1\ \mu m^{-1}$. (b) The evolution of the phonon spectra with changing the probing phonon wave vector defined by the incident light angle. The figure is adapted from Chun-Yu Huang et al., "Fine-tuning of the phonon spectrum and light – matter interactions in nanoscale pillar arrays," Nanoscale (in preparation, 2019).

The PxC sample in the current study is an array of pillars arranged in a square lattice and thus, possesses a 4-fold rotational symmetry. This means that the results of BMS experiment would be the same as the one presented in Figure 4-4 (a) if the sample is rotated about the axis normal to the sample by $\alpha = 90$ degrees. The frequency of the phonon modes, which are localized within the "hat" or "pillar" structure should not depend on the crystallographic direction of the PxC. This fact provides a tool for distinguishing the phonon spectrum changes due to the localization from that due to periodicity of the structure. Practically, it can be done by conducting BMS experiments at orientation angles, α, where $q_{\parallel}$ lies along directions other than the rotational symmetric directions. One should note that the orientation angle α is different from that of the incident laser light angle θ. The former defines the direction and the latter determines the magnitude of the phonon wave vector in BMS experiment, respectively. Figure 4-5 presents the results of the BMS experiment at constant phonon wave vector $q_{\parallel} = 18.1\ \mu m^{-1}$ along two different crystallographic directions of [110] ($\alpha = 0$, black curve) and [010] ($\alpha = 45°$, red curve), respectively. It is important to note that some phonon modes, which were observed along the [110] direction, have disappeared in the spectrum accumulated along the [010] direction. One can conclude that the modes, which are present in both spectra with the same frequency are spatially localized phonon modes. The modes that disappeared or changed their frequency can be the ones either resulting from the nano-pillar arrays' periodicity, via elastic coupling through the substrate, or at least affected by the periodicity.

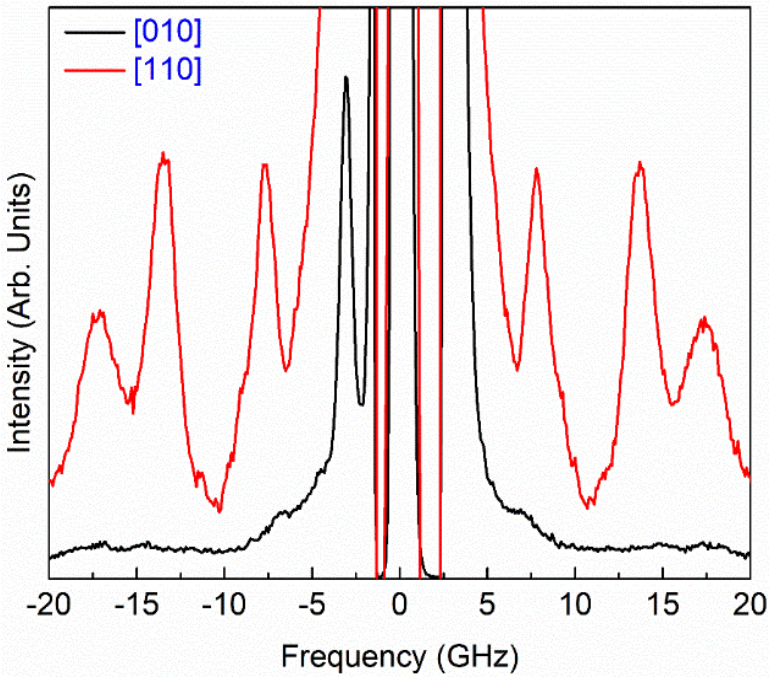

Figure 4-5: Brillouin-Mandelstam spectroscopy data for two different crystallographic directions in the same shape-engineered silicon nanoscale pillar array. Note that changing the orientation of the BMS scanning results in disappearance of some of the phonon peaks. The figure is adapted from Chun-Yu Huang et al., "Fine-tuning of the phonon spectrum and light – matter interactions in nanoscale pillar arrays," Nanoscale (in preparation, 2019).

Imposing the artificial periodicity, *e.g.* adding holes or nano-pillars to the silicon substrate, changes the BZ geometry. In our case, since the "pillar with hat" structures are arranged in a two-dimensional square lattice, the first BZ has a square geometry with the boundaries located at π/a, where $a = 500\ nm = 0.5\ \mu m^{-1}$ is the pitch, *i.e.* the distance between the central axis of two adjacent pillars along the [110] direction. Thus, the boundaries of the first BZ are located at $6.28\ \mu m^{-1}$ and $8.88\ \mu m^{-1}$, along the [110] and [010] directions, respectively. We conducted BMS experiments along the [110] and [010] crystallographic directions at various incident light angles ranging from $\theta = 18°$ to $\theta = 52°$, corresponding

to 7.3 $\mu m^{-1} \leq q_{\parallel} \leq 18.6\ \mu m^{-1}$, respectively. The experimental data, accumulated in this range of $q_{\parallel}$ values, cover the most part of the 2nd and higher order BZ's along the [110] direction, and part of the 1st and higher order BZ's along the [010] direction. The spectral position of the observed BMS peaks along the [110] and [010] directions are plotted as a function of $q_{\parallel}$ in Figure 4-6 (a-b). The frequency of the peaks does not depend on the $q_{\parallel}$, exhibiting almost a flat dispersion throughout the 1st and higher order BZ's. The phonon modes, which have the same frequency in both plots, are marked with the same symbol and colors. These modes are likely confined within the "pillar with hat" structures since their dispersion does not change as the periodicity changes by rotating the sample by $\alpha = 45°$.

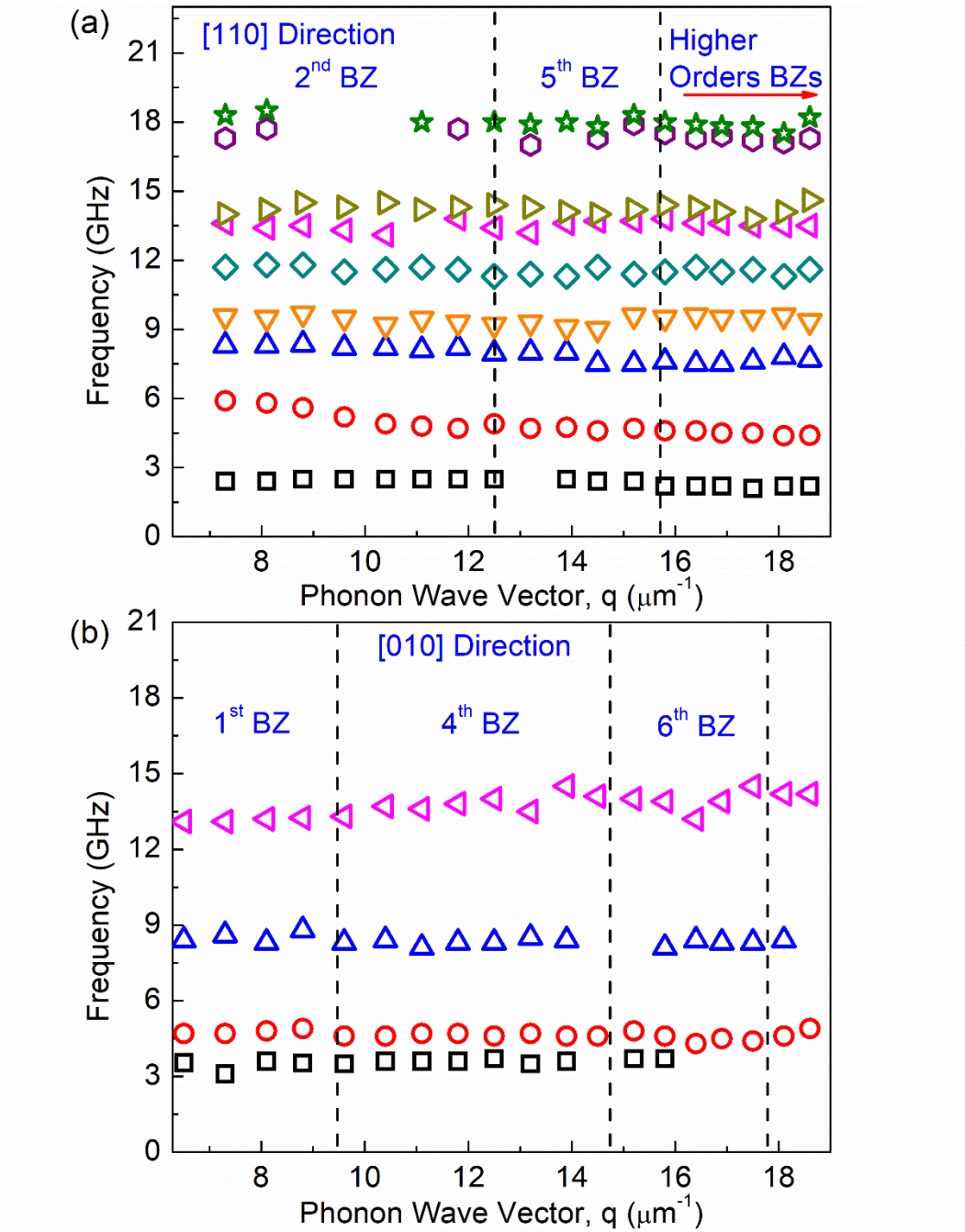

Figure 4-6: Phonon dispersion in the shape-engineered silicon nanoscale pillar array shown for (a) [110] and (b) [010] crystallographic directions. Note that the number of phonon branches decreases from nine to four with the direction change. The figure is adapted from Chun-Yu Huang et al., "Fine-tuning of the phonon spectrum and light – matter interactions in nanoscale pillar arrays," Nanoscale (in preparation, 2019).

4.3.2 Theoretical Analysis and Finite Element Method Simulations

To better understand the nature of the flat-band phonons, we calculated the phonon dispersion and displacement patterns for the silicon "pillar with hat" structures using the finite element modeling (FEM) implemented in COMSOL Multiphysics package. The pillars were modeled as part of a 2D periodic arrays, repeated along the X-Y plane. Each pillar is allowed to have free vibrations along the growth direction ($+z$), whereas the back part of the bulk substrate has a fixed boundary condition. The equation of motion for this phononic structure can be written from the second-order elastic continuum theory as $\rho(\partial^2 u(\mathbf{r})/\partial t^2) = \partial \mathrm{S}(\mathbf{r})/\partial x_i$ where ρ is the mass density and $u(\mathbf{r})$ is the displacement vector at coordinate $\mathbf{r}$. The stress tensor $\mathrm{S}(\mathbf{r})$ can be obtained from displacement by $S_{ij} = C_{ijkl}\,\varepsilon_{kl}$, where $\varepsilon(\mathbf{r}) = [(\nabla \mathbf{u})^{\mathrm{T}} + (\nabla \mathbf{u})]/2$ is the elastic strain tensor. For this study, C_{ijkl}, the coefficients for silicon are assumed to be isotropic in both substrate and pillars. To obtain the solution of the elasticity equation in the frequency domain, the simulation geometry is discretized using finite element scheme $\rho\omega^2 u = \nabla . S$, where ω is the Eigen frequency. Free surface boundary conditions are applied at all outer facets of the pillar as well as at the top surface, using $\varepsilon_{ij} n_j = 0$, where n_j is the outward normal unit-vector. To simulate the effect of additional hat-like structure on the phonon properties, we use a star-like protrusion on top of the pillar using the dimensions carefully extracted from the SEM images. The dimensions of the actual nanostructures have been determined from the SEM images under different angles. The schematic is shown in Figure 4-1 (a-b) was used for the modeling. The simulation results are presented in Figure 4-7 (a-b) for the [110] and [010]

crystallographic directions, respectively. The calculated dispersion reveals numerous phonon polarization branches with the flat dispersion in both crystallographic directions, consistent with the experimental data. At higher frequencies, the phonon dispersion becomes a “spaghetti” of many phonon bands crossing and anti-crossing each other, making a direct comparison with the experiment impossible. It is important to note that these quasi-optical phonon modes are all hybridized in nature, which makes them BMS active, with the high degree of confidence. The hybrid modes have vibrational displacement components perpendicular to the probing phonon wave vector, which is a required condition for being BMS observable. The displacement profiles of some BMS activated modes along [110] direction is presented in Figure 4-8.

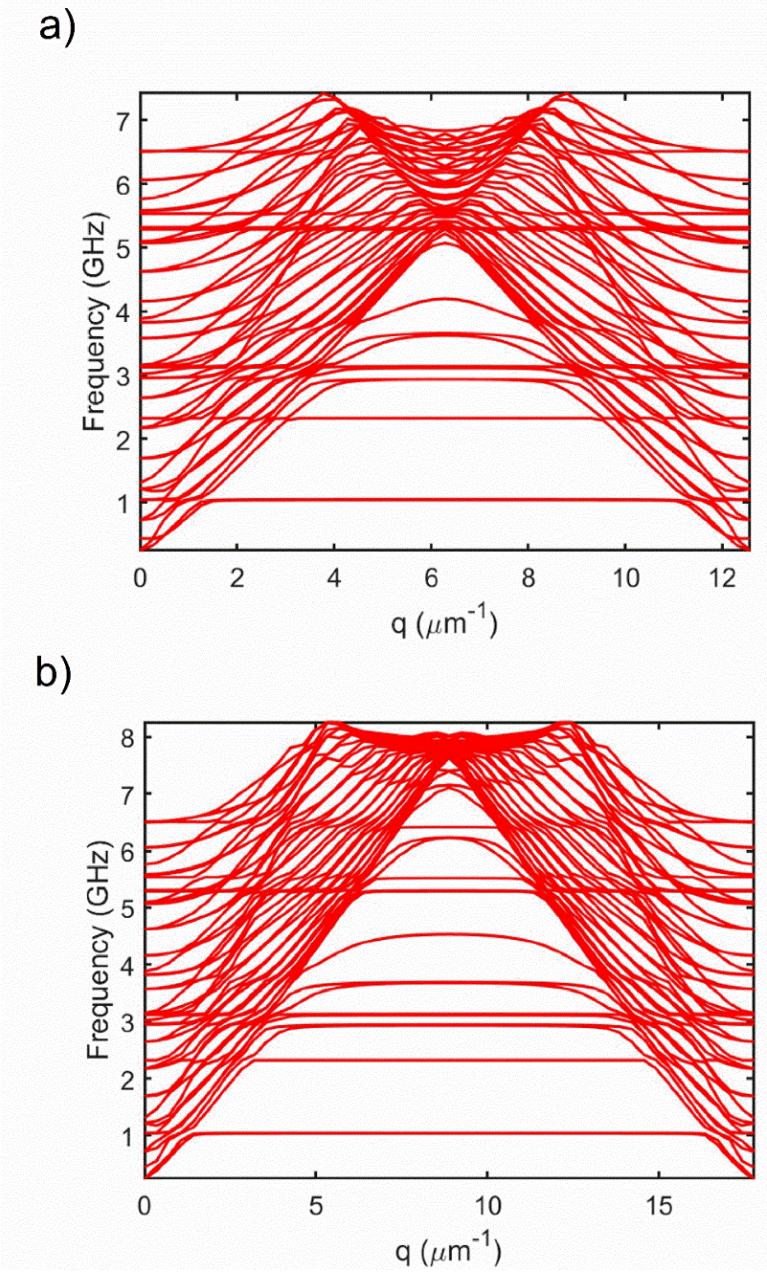

Figure 4-7: Calculated phonon dispersion for the pillar structure with similar geometry as the experimental samples. The data are shown for (a) [110] direction and (b) [010] directions. The figure is adapted from Chun-Yu Huang et al., "Fine-tuning of the phonon spectrum and light – matter interactions in nanoscale pillar arrays," Nanoscale (in preparation, 2019). The simulations are courtesy of T. Debnath and Dr. Roger Lake, UC Riverside.

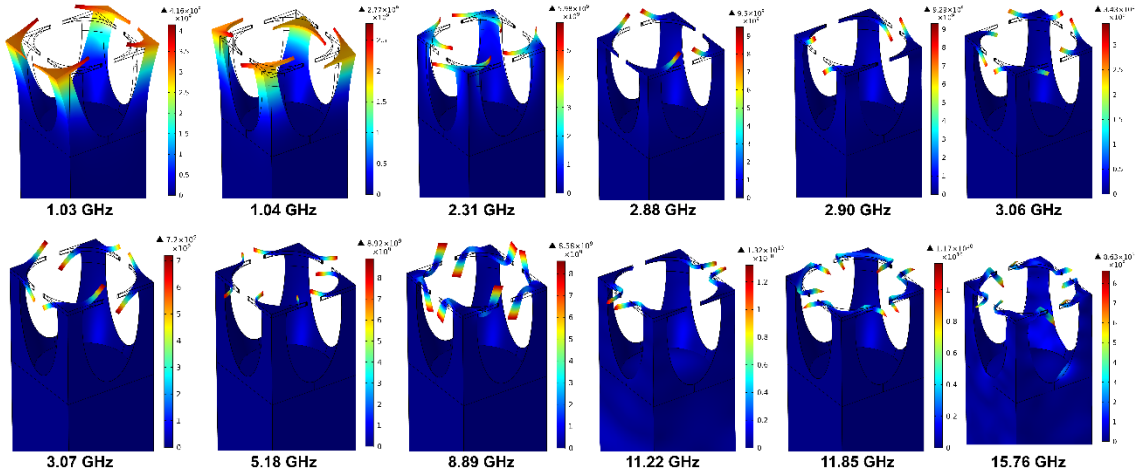

Figure 4-8: Vibrational displacement profile of BMS-active modes along [110] direction. The red color corresponds to stronger displacement. The figure is adapted from Chun-Yu Huang et al., "Fine-tuning of the phonon spectrum and light – matter interactions in nanoscale pillar arrays," Nanoscale (in preparation, 2019). The simulations are courtesy of T. Debnath and Dr. Roger Lake, UC Riverside.

4.3.3 Optical Characterization via VASE

The optical characteristics of the shape-engineered silicon nano-pillar arrays have determined using VASE (J.A. Woollam Co.) along the two crystallographic directions at the incident light angles $\beta = 50°, 55°, 60°, 65°$. The details of the Mueller ellipsometry have been explained in detail elsewhere [16]. Representative spectra of the Muller matrix elements at $\beta = 50°$ for both directions are presented in Figure 4-9. The Mueller matrix elements of the "pillar with hat" structures reveal multiple large-amplitude abrupt variations for the wavelengths below $\lambda < 800$ nm. The variations are different for two different crystallographic directions. The spectrum of silicon substrate is on a contrary characterized by very smooth change in the optical parameters. In ellipsometry, the Muller matrix is related to the ellipsometric functions of ψ and Δ as:

$$\mathbf{M} = \begin{bmatrix} 1 & -N & 0 & 0 \\ -N & 1 & 0 & 0 \\ 0 & 0 & C & S \\ 0 & 0 & -S & C \end{bmatrix}. \quad (4\text{-}1)$$

Here $N = \cos 2\psi$ and $C = \sin 2\psi \cos \Delta$ and $S = \sin 2\psi \sin \Delta$, respectively. All the indices are normalized with respect to the m_{11} element. The strong variations in the Muller matrix elements in the relevant wavelength interval, variation differences for two crystallographic directions, and a contrast with the optical properties of the reference silicon substrate indicate that the nano-pillar arrays act as PtC as well.

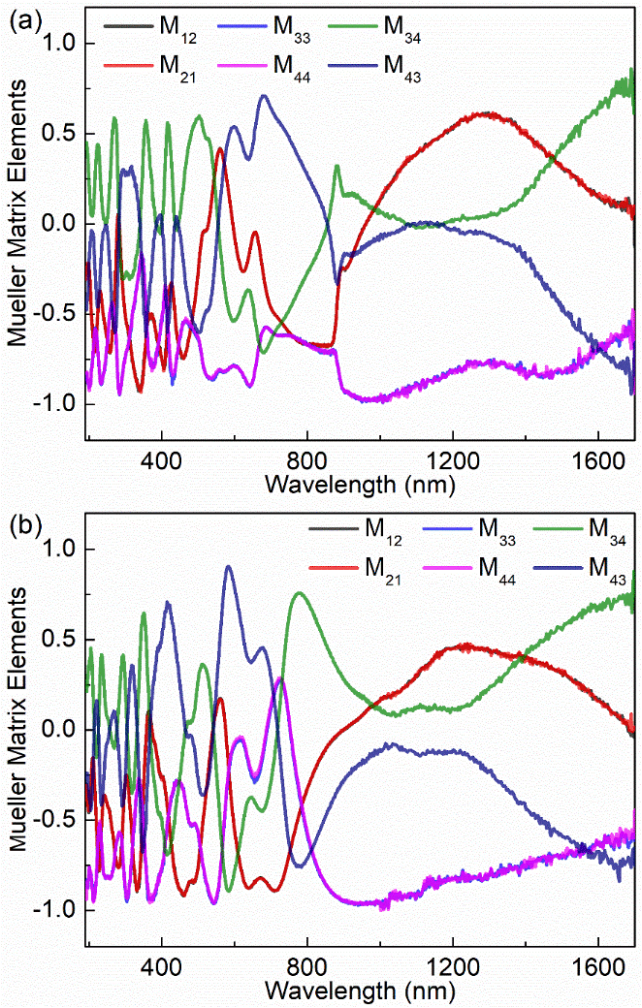

Figure 4-9: Ellipsometry spectra for the shape-engineered silicon nanoscale pillar array for (a) [110] quasi-crystallographic direction and (b) [010] quasi-crystallographic direction. Changing the orientation of the phononic – photonic crystal results in different interaction of the structure with light. The figure is adapted from Chun-Yu Huang et al., "Fine-tuning of the phonon spectrum and light – matter interactions in nanoscale pillar arrays," Nanoscale (in preparation, 2019).

4.4 Conclusions

In conclusion, we used BMS and VASE to demonstrate that a specially designed nanoscale "pillar with hat" periodic silicon structures reveal the properties of both phononic and

photonic crystals. Acoustic phonon states can be tuned by external boundaries, either as a result of phonon confinement effects in individual nanostructures, or as a result of artificially induced external periodicity. The shape of the nanoscale pillars was engineered to ensure the interplay of both effects. Our BMS data indicate strong flattening of the acoustic phonon dispersion in the frequency range from 2 GHz to 20 GHz and the phonon wave vector extending to the higher order BZs. The specifics of the phonon dispersion dependence on the pillar arrays orientation suggest the presence of both periodic modulation and spatial localization effects for the acoustic phonons. Our results suggest that smart engineering of the size and shape of the pillars enhances the tuning capability for phonon dispersion, which can be changed via spatial localization of confined phonons or pillar periodicity.

References:

[1] J.R. Sandercock, Trends in brillouin scattering: Studies of opaque materials, supported films, and central modes, Light Scatt. Solids III. 51 (1982) 173–206. https://doi.org/10.1007/3540115137_6.

[2] P. Mutti, C.E. Bottani, G. Ghislotti, M. Beghi, G.A.D. Briggs, J.R. Sandercock, Surface Brillouin scattering—Extending surface wave measurements to 20 GHz, in: A. Briggs (Ed.), Adv. Acoust. Microsc., Springer US, 1995: pp. 249–300. https://doi.org/10.1007/978-1-4615-1873-0_7.

[3] E. Alonso-Redondo, L. Belliard, K. Rolle, B. Graczykowski, W. Tremel, B. Djafari-Rouhani, G. Fytas, Robustness of elastic properties in polymer nanocomposite films examined over the full volume fraction range, Sci. Rep. 8 (2018) 16986. https://doi.org/10.1038/s41598-018-35335-1.

[4] F. Kargar, S. Ramirez, B. Debnath, H. Malekpour, R.K. Lake, A.A. Balandin, Acoustic phonon spectrum and thermal transport in nanoporous alumina arrays, Appl. Phys. Lett. 107 (2015) 171904. https://doi.org/10.1063/1.4934883.

[5] B. Graczykowski, M. Sledzinska, F. Alzina, J. Gomis-Bresco, J.S. Reparaz, M.R. Wagner, C.M. Sotomayor Torres, Phonon dispersion in hypersonic two-dimensional phononic crystal membranes, Phys. Rev. B. 91 (2015) 75414. https://doi.org/10.1103/PhysRevB.91.075414.

[6] D. Yudistira, A. Boes, B. Graczykowski, F. Alzina, L.Y. Yeo, C.M. Sotomayor Torres, A. Mitchell, Nanoscale pillar hypersonic surface phononic crystals, Phys. Rev. B. 94 (2016) 094304. https://doi.org/10.1103/PhysRevB.94.094304.

[7] T. Still, R. Sainidou, M. Retsch, U. Jonas, P. Spahn, G.P. Hellmann, G. Fytas, The “Music” of core−shell spheres and hollow capsules: Influence of the architecture on the mechanical properties at the nanoscale, Nano Lett. 8 (2008) 3194–3199. https://doi.org/10.1021/nl801500n.

[8] M.H. Kuok, H.S. Lim, S.C. Ng, N.N. Liu, Z.K. Wang, Brillouin study of the

quantization of acoustic modes in nanospheres, Phys. Rev. Lett. 90 (2003) 255502. https://doi.org/10.1103/PhysRevLett.90.255502.

[9] J. Cuffe, E. Chávez, A. Shchepetov, P.-O. Chapuis, E.H. El Boudouti, F. Alzina, T. Kehoe, J. Gomis-Bresco, D. Dudek, Y. Pennec, B. Djafari-Rouhani, M. Prunnila, J. Ahopelto, C.M. Sotomayor Torres, Phonons in slow motion: Dispersion relations in ultrathin Si membranes, Nano Lett. 12 (2012) 3569–3573. https://doi.org/10.1021/nl301204u.

[10] F. Kargar, B. Debnath, J.-P. Kakko, A. Saÿätjoki, H. Lipsanen, D.L. Nika, R.K. Lake, A.A. Balandin, Direct observation of confined acoustic phonon polarization branches in free-standing semiconductor nanowires, Nat. Commun. 7 (2016) 13400. https://doi.org/10.1038/ncomms13400.

[11] B. Hillebrands, C. Mathieu, M. Bauer, S.O. Demokritov, B. Bartenlian, C. Chappert, D. Decanini, F. Rousseaux, F. Carcenac, Brillouin light scattering investigations of structured permalloy films, J. Appl. Phys. 81 (1997) 4993–4995. https://doi.org/10.1063/1.364881.

[12] M.M. Lacerda, F. Kargar, E. Aytan, R. Samnakay, B. Debnath, J.X. Li, A. Khitun, R.K. Lake, J. Shi, A.A. Balandin, Variable-temperature inelastic light scattering spectroscopy of nickel oxide: Disentangling phonons and magnons, Appl. Phys. Lett. 110 (2017) 202406. https://doi.org/10.1063/1.4983810.

[13] J.R. Sanderocock, Light scattering from surface acoustic phonons in metals and semiconductors, Solid State Commun. 26 (1978) 547–551. https://doi.org/http://dx.doi.org/10.1016/0038-1098(78)91307-8.

[14] J.R. Sandercock, Brillouin-scattering measurements on silicon and germanium, Phys. Rev. Lett. 28 (1972) 237–240. https://doi.org/10.1103/PhysRevLett.28.237.

[15] R. Loudon, Theory of surface-ripple Brillouin scattering by solids, Phys. Rev. Lett. 40 (1978) 581–583. https://doi.org/10.1103/PhysRevLett.40.581.

[16] T. Brakstad, M. Kildemo, Z. Ghadyani, I. Simonsen, Dispersion of polarization

coupling, localized and collective plasmon modes in a metallic photonic crystal mapped by Mueller Matrix Ellipsometry, Opt. Express. 23 (2015) 22800. https://doi.org/10.1364/oe.23.022800.